Monthly Notices of the ROYAL ASTRONOMICAL SOCIETY

MNRAS **548,** 1–22 (2026)
Advance Access publication 2026 March 31

https://doi.org/10.1093/mnras/stag619

Infrared synchrotron emission in the soft state of GX 339–4 and the mid-infrared/X-ray luminosity plane of black hole X-ray binaries

P. Gandhi [1★] D. M. Russell [2] M. C. Baglio [3] Y. Bhargava [4,5] R. Duncan,[6,7] A. Gúrpide [1] C. O. Heinke [8] C. Knigge [1] K. S. Long,[9,10] T. J. Maccarone,[11] G. Mastroserio,[12] T. D. Russell [13] A. W. Shaw [14] A. J. Tetarenko [15] F. M. Vincentelli [1,16] E. S. Borowski [17] D. A. H. Buckley [18] P. Casella [19] C. Dashwood Brown,[1] G. C. Dewangan [20] R. I. Hynes [17] S. Markoff [6,7] J. A. Tomsick [21] K. Alabarta [2] F. Carotenuto [19] E. Carver [15] N. Castro-Segura,[1] P. Charles,[1] F. Lewis [22,23] J. A. Paice [24] D. Pawar [25] M. E. Ressler [26] S. K. Rout [2] P. Saikia [2] T. Shahbaz [27,28] and G. R. Sivakoff [8] (JWST Timing Consortium)

Affiliations are listed at the end of the paper

Accepted 2026 March 27. Received 2026 February 27; in original form 2025 September 30

ABSTRACT

Progress in understanding accreting black holes remains hampered by a lack of sensitive coordinated multiwavelength observations. In particular, the mid-infrared (MIR) regime remains ill-explored except for jet-dominant states. Here, we present comprehensive follow-up of the black hole X-ray binary GX 339–4 during a bright disc-dominated state in its 2023/24 outburst as part of a multiwavelength campaign coordinated around *James Webb Space Telescope* (*JWST*)/MIRI. The X-ray properties are fairly typical of soft accretion states with no significant X-ray variability, though with a weak high-energy Comptonized power-law tail. The source is significantly detected, and variable, across 5–10 μm, at a faint mean flux level. This requires any MIR compact jet contribution to be suppressed by $\gtrsim 300$ relative to previous hard-state detections. The MIRI spectrum can be described as a simple power-law with slope $\alpha = +0.39 \pm 0.07$ ($F_\nu \propto \nu^\alpha$), but matches neither the radio/sub-mm nor the optical broad-band slopes. Synchrotron radiation from the same medium responsible for high-energy Comptonization can self-consistently account for the observed MIRI spectral-timing behaviour, offering new constraints on the physical conditions in the soft-state accretion disc atmosphere/corona. Alternative explanations, including a circumbinary disc, emission from a warm wind, or transient compact jet activity fail to cleanly explain either the spectral properties or the variability. Multiwavelength timing cross-correlations show a puzzlingly long MIR lag relative to the optical, though at limited significance. We compile archival MIR and X-ray luminosities of transient black hole systems, including previously unreported detections of GX 339–4. These trace the evolution of the MIR-to-X-ray flux ratio with accretion state, and also reveal high MIR luminosities for GX 339–4 across all states.

Key words: stars: black holes – infrared: general – X-rays: binaries.

1 INTRODUCTION

X-ray binaries (XRBs) are ideal targets for studying transient multiwavelength emission arising from accretion activity. They spend most of their lives in a state of low-level 'quiescence', as a result of weak accretion on to the central compact object (either a black hole or a neutron star) from the binary companion (e.g. S. Campana et al. 1998; J. P. Lasota 2000; C. O. Heinke et al. 2003). This is punctuated by occasional accretion 'outbursts' lasting months to years and characterized by a prolific rise in radiation output and flux variability (e.g. R. J. H. Dunn et al. 2010). Several physical components including the accretion disc, collimated and uncollimated outflows, the companion star, and more can contribute to the observed multiwavelength emission (e.g. C. Done, M. Gierliński & A. Kubota 2007). Spectral-timing observations offer the possibility to disentangle these components based on their differing scales and characteristic variability time-scales (e.g. P. Uttley & P. Casella 2014).

The infrared (IR) spectral regime spans a broad wavelength range of approximately 1–100 μm. A variety of thermal and non-thermal processes can contribute to the IR emission of XRBs, as discussed below. The shortest IR wavelengths, $\lesssim 2.5$ μm adjacent to the optical, are the best studied because they are accessible through atmospheric transmission windows and have benefitted from detector technology maturation since the 1990s. At longer wavelengths, thermal background noise rises by orders of magnitude, making observations progressively more difficult.

★ E-mail: poshak.gandhi@soton.ac.uk

In the mid-infrared (MIR) spectral regime ($\lambda \sim 5$–$30\,\mu$m), only very few, and relatively narrow, atmospheric windows are accessible from the ground. Observations in this regime typically rely on impurity-band conduction arrays, such as arsenic-doped silicon detectors cooled to a few kelvin. At far-IR wavelengths ($\lambda \gtrsim 30\,\mu$m) the Earth's atmosphere is essentially opaque, and different detector technologies, including bolometers and transition-edge sensors, are required to detect the correspondingly low photon energies. As a consequence, XRBs remain comparatively poorly explored in both the mid- and far-IR regimes.

There have been efforts to detect XRBs with all MIR missions, though the poor spatial resolution of historical IR missions made robust counterpart identification difficult (H. A. Smith, J. H. Beall & M. R. Swain 1990). The ISOCAM camera aboard the *Infrared Space Observatory* (*ISO*) detected several bright or persistent sources (I. F. Mirabel et al. 1996; L. Kaper et al. 1998; Y. Fuchs, I. F. Mirabel & A. Claret 2003). The era of *Spitzer* and *WISE* opened up MIR studies of XRBs more widely, with many photometric detections in quiescence as well as in outburst (e.g. S. Migliari et al. 2006; E. Gallo et al. 2007; S. Wachter 2008; P. Gandhi et al. 2011b; X. Wang & Z. Wang 2014; C. John et al. 2024). Spectroscopic detections of bright and persistent sources also followed (Y. Fuchs, L. Koch Miramond & P. Ábrahám 2006; F. Rahoui et al. 2010, 2011). At longer far-IR wavelengths, notable studies include those of S. Corbel et al. (2013b) who presented *Herschel* 70- and 160-μm photometric detections of a BHXB during outburst – the same source studied herein – highlighting complex broad-band jet synchrotron spectral slopes, and those of T. E. Harrison et al. (2014) and M. Servillat et al. (2014) who detected dust and possible wind signatures around neutron-star XRBs.

Transient outbursts grow from quiescence through the 'hard' state during which the hot accretion flow close to the central source strengthens (e.g. R. P. Fender, T. M. Belloni & E. Gallo 2004; C. Done et al. 2007). Both quiescence and the hard state are typically dominated by non-thermal emission processes, including synchrotron radiation in the MIR (S. Migliari et al. 2006; E. Gallo et al. 2007; F. Rahoui et al. 2011; P. Gandhi et al. 2011b). Near peak, this can approach flux levels bright enough to be detectable from the ground in the MIR 10 μm transmission window (J. Paradijs et al. 1994; D. M. Russell et al. 2013b; M. C. Baglio et al. 2018; F. M. Vincentelli et al. 2021; P. Saikia et al. 2022; C. Echiburú-Trujillo et al. 2024). Dissipative plasma shocks within compact jets are able to account for the broad-band spectral as well as timing properties observed during the hard state (R. D. Blandford & A. Königl 1979; S. Markoff, H. Falcke & R. Fender 2001; J. Malzac 2013; D. M. Russell et al. 2013; J. Malzac 2014; P. Gandhi et al. 2016, 2017). We note that the presence of circumbinary dust discs has also been proposed as the primary driver of the MIR radiation in quiescence (M. P. Muno & J. Mauerhan 2006), a point that we return to later.

By contrast, transient XRB detections are even sparser in the MIR during the 'soft' accretion state, when thermal emission from a fully active accretion disc dominates the electromagnetic output. Radio jet emission appears to be heavily suppressed in these soft states (D. M. Russell et al. 2011; A. P. Rushton et al. 2016; T. D. Russell et al. 2020; C. John et al. 2024), though some transient compact radio jets have been observed during this phase (D. M. Russell et al. 2020). It remains unclear whether this is a result of a complete failure to launch the jet in the soft state, or a result of inefficient (re-)acceleration of collimated plasma as it travels away from the central source, due to e.g. a change in the jet magnetic field configuration. Current constraints on optical and IR flux suppression in the soft states of most sources could support either scenario (e.g. D. M. Russell et al. 2006).

Table 1. Physical parameters of GX 339–4 adopted in this work.

Distance d	8 (> 5) kpc
Orbital period P	1.7587 ± 0.0005 d
Black hole mass $M_{\rm BH}$	6 (4–11) $M_\odot$
Inclination i	50 (40–60) deg
Mass ratio $q(= M_2/M_1)$	0.18 ± 0.05
Binary separation a	11.77 $R_\odot$ = 27.3 lt-sec
Donor Roche Lobe radius $R_{\rm L}$	3.88 $R_\odot$ = 9.1 lt-sec
Extinction $A_{\rm V}$	3.5 ± 0.5 mag

Note. Approximate ranges or constraints are noted in brackets. 1σ uncertainties are stated for measured/adopted quantities, when available (P. Gandhi et al. 2011b; M. Heida et al. 2017; A. A. Zdziarski et al. 2019).

Here, we present one of the most sensitive MIR detections of a black hole XRB in a disc-dominated accretion state. This enables deep constraints on the inner jet behaviour during this state, as well as allowing us to test for the presence of other components often invoked in the IR such as dust, a circumbinary disc (CBD), and the companion star.

For this purpose, we used *James Webb Space Telescope* (*JWST*) to observe the XRB GX 339–4, a dynamically confirmed black hole system with an orbital period $P = 1.759$ d (R. I. Hynes et al. 2003; M. Heida et al. 2017), located at a minimum heliocentric distance $d \gtrsim 5$ kpc (R. I. Hynes et al. 2004; M. Heida et al. 2017). GX 339–4 undergoes frequent bright transient outbursts, as a result of which it has become a cornerstone of multiwavelength XRB studies over many decades (K. Makishima et al. 1986; S. Corbel & R. P. Fender 2002; T. Belloni et al. 2005; R. J. H. Dunn et al. 2008; P. Gandhi et al. 2008, 2010; P. Casella et al. 2010; S. Corbel et al. 2013a; F. M. Vincentelli et al. 2019). Previous mid-IR photometric detections of the source have been reported (P. Gandhi et al. 2011b; X. Wang & Z. Wang 2014; C. John et al. 2024) during the hard outbursting state. No MIR *spectroscopic* observations have been reported so far.

The system parameters remain under debate, with a black hole mass range of $M_{\rm BH} = 4$–$11\,M_\odot$ (A. A. Zdziarski, J. Ziółkowski & J. Mikołajewska 2019). Some of the key parameters, including the values adopted in this work, are listed in Table 1. When available or computed herein, quoted uncertainties correspond to 68 per cent intervals throughout the paper, unless stated otherwise.

2 OBSERVATIONS

2.1 *JWST*/MIRI

We first triggered *JWST* in 2022 September, during the rising part of an outburst at that time as part of a Target-of-Opportunity Phase Cycle 1 program (ID 1586). The observation was unsuccessful due to a guide star acquisition error. The cause of the failure was analysed by the STScI mission team and attributed to a faulty entry in the mission's guide star catalogue, which was later rectified by the mission team (WOPR 88542; STScI, private communication).

GX 339–4 was subsequently retriggered, and observed, on 2024 March 10 (MJD 60379) using MIRI (G. H. Rieke et al. 2015), set up for Slitless Low Resolution Spectroscopy (S. Kendrew et al. 2015). The SLITLESS PRISM sub-array was utilized to obtain continuous time-series monitoring for an on-source stare lasting about 2 h. Source acquisition was performed using an offset pointing

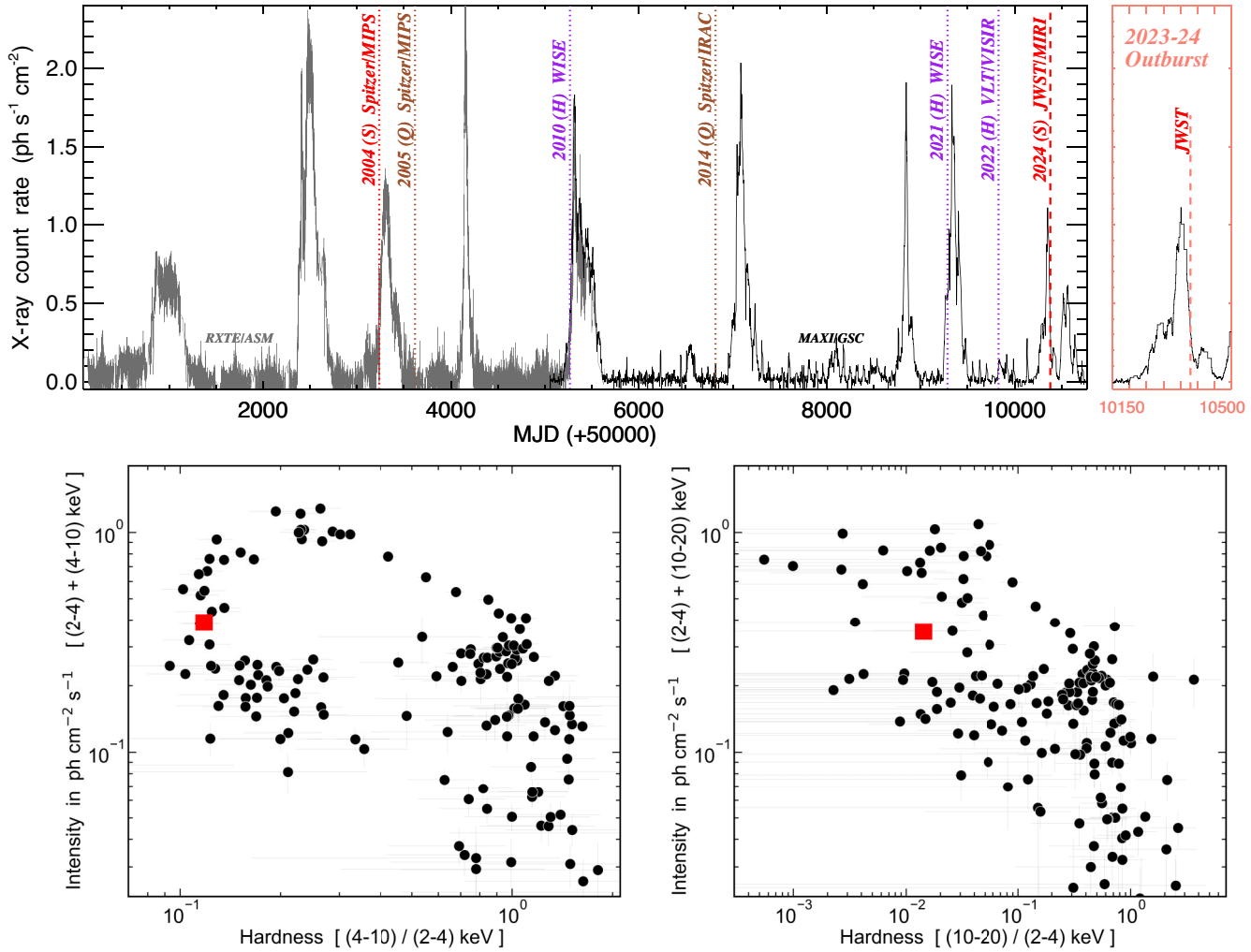

Figure 1. *Top*: long-term X-ray light curve of GX 339–4, with all known historical MIR observational epochs annotated and denoted. Recent X-ray data are from the MAXI Gas Slit Camera (GSC), covering the 2–20 keV band. Pre-MAXI data from *RXTE*/ASM are plotted in grey before ∼ MJD 55 000, normalized to the MAXI photon flux by multiplying by a factor of 0.032, which converts between the respective full energy bands of the two cameras assuming a 1 keV blackbody model approximately appropriate for outburst peaks. X-ray accretion state is stated in parentheses: soft (S), hard (H), and quiescent (Q) and colour-coded in red, purple, and brown, respectively. The small panel on the right shows a zoom-in around the 2023–24 outburst when *JWST* observed the source. *Bottom*: X-ray HIDs using MAXI data, covering the 2023/24 outburst. The panels differ in the definition of the harder band: (4–10 keV) on the left and (10–20 keV) on the right, highlighting differences relevant to the dominance of the high-energy power-law tail. The red point denotes the observation date coinciding with *JWST*.

slew from the nearby bright star *Gaia* DR3 5938658049055243136 located 13.5 arcsec to the south-east of GX 339–4.

The first on-source science frame began at UT 06:36:16.31. Observations were performed in the standard non-destructive FASTR1 mode (cf. M. E. Ressler et al. 2015; A. Dyrek et al. 2024), for a total of nINT = 1470 integrations (each 4.77 s long, with a tagged-on reset dead-time of approximately 0.16 s). The time of the final science frame was UT 08:37:03.78.

Data were processed using the latest *JWST* pipeline, version 1.17, available at the time of writing, with calibration data base context 1322. The pipeline conducts several steps of calibration and artefact correction to ensure a linear signal response and to flag outliers. There are still a number of shortcomings in the pipeline (e.g. background uncertainties are not included within the final reported errors, there appears to be excess r.m.s. variability towards the red end of the bandpass), which have been discussed in our prior work (P. Gandhi et al. 2025). These were manually implemented where possible and relevant for the analysis below. Other relevant pipeline settings were adopted from our prior work. We experimented with modifying parameters (e.g. the jump step detection threshold, which can identify sudden ramp changes due to cosmic rays), but these did not impact the final extraction significantly.

The source was found to be faint, but clearly detected in all integrations. The signal weakens towards longer wavelengths where calibrations remain uncertain, and background artefacts become more difficult to account for. We thus restricted our analysis to the wavelength regime of 5–10 μm.

JWST caught GX 339–4 during a state characterized by strong disc emission, as the source was declining from the peak of its 2023–24 outburst (Fig. 1). The overall outburst turned out to be weaker compared to prior prominent outbursts, though the source still completed a full traversal of the X-ray hardness–intensity diagram (HID) common to this system (e.g. T. Belloni

et al. 2005). The source was classified as being in the X-ray soft state by G. Mastroserio et al. (2025), who used MAXI X-ray sky monitor hardness ratios to place it in a region of the HID characteristic of soft sources (Fig. 1 bottom panels). Their detailed spectral analysis confirmed the presence of a strong accretion disc, together with a Comptonized tail at energies above 10 keV carrying ∼1 per cent of the X-ray broad-band flux. Furthermore, X-ray variability was found to be weak and no significant X-ray polarization was detected, self-consistent with a soft state. Our analysis presented later in this paper confirms these general properties. The panel on the bottom-right of Fig. 1 shows hardness values based on the highest-energy MAXI band (10–20 keV, as opposed to 4–10 keV on the bottom-left). The scatter in this panel is more sensitive to the strength of the high-energy power-law tail than HIDs based on lower energy bands, demonstrating some scatter within this accretion state, which should be kept in mind for any detailed comparisons of the accretion state with other observations.

2.2 Multiwavelength campaign

We arranged for several multiwavelength facilities to coordinate with the *JWST* observation. Due to a failure in unrelated observations scheduled just prior to ours, the *JWST* schedule changed dynamically and the GX 339–4 observing window slid forward by approximately 2 h without our knowledge, resulting in imperfect overlap with some facilities. Nevertheless, we were able to build in sufficient redundancy within our campaign to ensure strict simultaneity with a few facilities, and quasi-simultaneity with the rest to within 1 d (and usually just a few hours) across the electromagnetic spectrum. A figure denoting the coodination timeline may be found in Appendix A.

2.2.1 Swift

The X-ray Telescope (D. N. Burrows et al. 2005) onboard the *Neil Gehrels Swift Observatory* (N. Gehrels et al. 2004) observed the source for a duration of 1029.6 s, starting at MJD 60379.45545 (ObsID 00014052219) in windowed timing (WT) mode. This observation began 2.3 h after the end of the *JWST* observation.

Data products were extracted using UK Swift tools (P. A. Evans et al. 2009). The spectrum was grouped to a minimum of 20 counts for fitting. The source was bright, with a net count rate of 224 ct s^{-1} over the 0.3–10 keV band, suggesting pile-up even in WT mode (the automated extraction corrects for this using an annulus). Spectral analysis was restricted to 1–10 keV, in order to avoid residuals related to bright absorbed sources at soft energies..[1]

2.2.2 NuSTAR

The *Nuclear Spectroscopic Telescope Array* (*NuSTAR*; F. A. Harrison et al. 2013) observed GX 339–4 for approximately 20 ks starting on 2024 March 10 02:30 UTC (ObsID: 80902342002, PI: Shaw). Data were reprocessed with the FTOOL `nupipeline` included in HEASOFT v6.35.1 (NuSTARDAS v2.1.5). Event files from each focal plane module (FPMA and FPMB) were corrected to the Solar system barycentre using `barycen`. Source spectra and light curves were extracted from FPMA and FPMB using a circular region of radius 70 arcsec centred on the source and background spectra and light curves were extracted from a circular region of the same size, centred on a source-free region on the same chip as GX 339–4. Spectral responses were generated using the FTOOL `nusproducts`. Light curves were binned into intervals of 4.93 s duration (closely matching the MIRI integration spacing), and spectra were grouped such that each bin contained a minimum of 20 counts.

2.2.3 LCO

Optical monitoring of GX 339–4 was performed with telescopes at the Las Cumbres Observatory (LCO) before, during, and after the *JWST* observation. Data were taken as part of a monitoring campaign of ∼50 low-mass XRBs coordinated with the Faulkes Telescope Project (F. Lewis et al. 2009; F. Lewis 2018). GX 339–4 has been regularly monitored by the 2-m Faulkes Telescope South (at Siding Spring Observatory, Australia), which is part of LCO, since 2007 (e.g. D. M. Russell et al. 2008; M. Cadolle Bel et al. 2011). To increase the cadence close in time to the *JWST* observation, we observed with LCO on 12 epochs within ±2 d of *JWST*. The 1-m LCO network telescopes at Cerro Tololo Inter-American Observatory (Chile), the South African Astronomical Observatory (SAAO; South Africa), and Siding Spring Observatory were used, as well as the 2-m at Siding Spring Observatory (see also K. Alabarta et al. 2024, for LCO magnitudes reported in the weeks–months prior to the *JWST* observation). Images were taken using the Bessel B, V, and R filters (Vega magnitudes), the SDSS g', r', and i' filters (AB magnitudes), and Pan-STARRS z_s filter (AB magnitudes).

To reduce and analyse the images, the real-time data analysis pipeline, XB-NEWS (the X-ray Binary New Early Warning System; see D. M. Russell et al. 2019; A. J. Goodwin et al. 2020), was used. The XB-NEWS pipeline downloads images of targets from the LCO archive soon after they are taken by the telescopes, and their associated calibration data. The pipeline then carries out quality control steps so that only good quality images are analysed, and produces astrometric solutions for each image using *Gaia* DR2 positions.[2] Aperture photometry was performed on all detected stars in each image, solving for zero-point calibrations between epochs (D. M. Bramich & W. Freudling 2012). The ATLAS All-Sky Stellar Reference Catalog (ATLAS-REFCAT2; J. L. Tonry et al. 2018) was adopted for flux calibration. Multi-aperture photometry (azimuthally averaged PSF profile fitting photometry, P. B. Stetson 1990) was also performed for point sources. We detect GX 339–4 with high significance. Modified Julian Dates and Barycentric Julian Dates at mid-exposure were output by XB-NEWS. For the broad-band spectrum, all measurements within ±1.0 d of *JWST* were retained and averaged in each filter.

2.2.4 REM

We observed GX 339–4 in the H band with the 60-cm Robotic Eye Mount (REM) telescope at La Silla (Chile) on 2024 March 10 (MJD 60379) under good sky conditions, strictly simultaneously with *JWST*, as part of a monitoring campaign during the ongoing outburst. Observations were conducted between 06:51:07 UT and 06:53:37 UT and consisted of one set of exposures composed of

[1] https://www.swift.ac.uk/analysis/xrt/digest_cal.php#abs

[2] https://www.cosmos.esa.int/web/gaia/dr2

five dithered 30-s integrations, which were combined for optimal background subtraction.

We performed aperture photometry using `daophot` (P. B. Stetson 1987), with an aperture radius of 1.5 times the average full width at half-maximum of the flux profiles of the field stars. Flux calibration was performed using the 2MASS catalogue[3] (M. F. Skrutskie et al. 2006).

2.2.5 *HAWK-I*

Near-IR photometry in the K_s band was obtained with HAWK-I, an IR imager with 2×2 Hawaii 2RG detectors mounted at the Very Large Telescope UT-4 on Cerro Paranal, Chile (J.-F. Pirard et al. 2004). The observation ended up being strictly simultaneous with *JWST*.

Data were collected in Fast-phot mode, i.e. reducing the field of view to one stripe (2048 x 64 pixels) per detector. This mode allows to obtain data cubes of 250 frames, each with 0.125 s time resolution. The instrument rotation and pointing was set to place GX 339–4 and a bright reference star in the lower quadrant (Q1).

The average source flux was measured through aperture photometry with an annular background region, and absolute photometry was calibrated against the bright reference star. The average flux density was measured to be $F_{2.2\,\mu\mathrm{m}} = 0.55 \pm 0.05$ mJy. HAWK-I's fast-phot allows very rapid sub-second photometry, which requires dedicated calibration against changing seeing, and will be presented in future work.

2.2.6 *AstroSat*

AstroSat (K. P. Singh et al. 2014) observed GX 339–4 between 2024-03-10 10:51:45.5 and 2024-03-12 14:06:46.3 UTC (observation ID: A13_028T01_9000006122). To capture the broad-band evolution of the source, the Soft X-ray Telescope (SXT; K. P. Singh et al. 2017) and Large Area X-ray Proportional Counter (LAXPC; P. C. Agrawal et al. 2017; J. S. Yadav et al. 2017) observed the source in fast window (FW) and event analysis (EA) mode, respectively. To verify whether we detect any UV emission from the source, we also configured observations with the Ultra Violet Imaging Telescope (UVIT; S. N. Tandon et al. 2017, 2020) using various filters in the far-ultraviolet.

SXT level 2 data for individual orbits were downloaded from AstroBrowse[4] and merged using the JULIA tool `SXTMerger`. To mitigate core pile-up, spectra were extracted using an annular region confined to 1–4 arcmin. Additionally, light-curve analysis showed intervals of 0 counts during some 'good time' intervals, suggesting data drops during these segments, which were excluded. The final spectral analysis was conducted with a recommended 2 per cent systematic error included (e.g. Y. Bhargava et al. 2019, 2023). Noticing strong residuals close to 2 keV, we applied additional gain corrections, keeping the gain slope fixed at 1.0 and varying the gain offset parameter freely. For bright sources, the standard ARF shows additional residuals, which can be mitigated through dedicated modelling, and we utilized the ARF developed for the SXT observation of the bright transient MAXI J1820+070 (S. Banerjee et al. 2024). Since the extraction regions differ between the observations, this results in strong change in the cross-normalization constant for SXT (Table 2).

Table 2. Results of broad-band spectral fitting with an absorbed, irradiated, and Comptonized disc, a thermally emitting circumbinary disc and radio-emitting jet ejecta power law.

Component	Parameter		Units
	Nuclear absorption		
`tbabs`	$N_{\rm H}$	$6.8\,(\pm 0.2) \times 10^{21}$	cm^{-2}
	Irradiated and Comptonized disc		
`diskir`	$kT_{\rm disc}$	0.63 ± 0.01	keV
	Γ	$2.03^{+0.05}_{-0.04}$	
	$kT_{\rm e}$	300^{f}	keV
	$L_{\rm covr}/L_{\rm d}$	$4.1^{+0.1}_{-0.2} \times 10^{-2}$	
	$f_{\rm in}$	$0.28^{+0.02}_{-0.03}$	
	$r_{\rm irr}$	$1.000^{+0.002}_{-0.001}$	
	$f_{\rm out}$	$2^{+3}_{-1} \times 10^{-2}$	
	$\log r_{\rm out}$	$4.49^{+0.06}_{-0.07}$	
	norm	$2.7^{+0.1}_{-0.2} \times 10^{3}$	
`smedge`	$E_{\rm edge}$	$12.5^{+0.2}_{-0.1}$	keV
	Width W	$7.9^{+2.0}_{-1.2}$	keV
`gauss`	E	$6.56^{+0.07}_{-0.08}$	keV
	σ	$0.18^{+0.11}_{-0.09}$	keV
	norm	$1.9^{+1.2}_{-0.6} \times 10^{-4}$	$\mathrm{ph\,cm^{-2}\,s^{-1}}$
	Circumbinary disc		
`bbody`	$kT_{\rm dust}$	$6.5\,(\pm 0.4) \times 10^{-5}$	keV
	norm	$3.0\,(\pm 0.3) \times 10^{-6}$	$10^{36}\,\mathrm{erg\,s^{-1}\,kpc^{-2}}$
	Ejecta power law		
`cutoffpl`	Γ	$1.58^{+0.03}_{-0.04}$	
	norm	$8^{+4}_{-3} \times 10^{-5}$	$\mathrm{ph\,cm^{-2}\,s^{-1}\,keV^{-1}}$
	X-ray cross-normalization constants		
$C^{\rm FPMA}_{\rm FPMB}$	CONST	0.97 ± 0.01	
$C^{\rm FPMA}_{\rm SXT}$	CONST	$3.97^{+0.04}_{-0.05}$	
GAIN (SXT)[g]	slope	1.0^{f}	
	offset	$+\,66.2 \pm 0.5$	eV
$C^{\rm FPMA}_{\rm LAXPC}$	CONST	0.83 ± 0.02	
$C^{\rm FPMA}_{\rm XRT}$	CONST	$1.28^{+0.01}_{-0.02}$	
χ^2/dof		1650.9/1659	

Notes. The full model in `xspec` notation is `CONST(tbabs(smedge(diskir + gauss) + bbody + cutoffpl))`.
[u]unconstrained. [f]fixed.
[g]Additional gain offset allowance for *AstroSat*-SXT as a free variable.

LAXPCSOFTWARE22AUG15[5] (H. M. Antia et al. 2021; R. Misra, J. Roy & J. S. Yadav 2021) was used to process level 1 LAXPC data, including uniform merging of individual orbits and gain correction, and extraction of spectra and responses. Due to the steep spectral slope of the source in the operational energy range of LAXPC, we extracted the data only from layer 1 of the instrument to minimize background contribution. As a result, the LAXPC spectra are usable only in the 3–20 keV energy range. We included a recommended 3 per cent additional systematic error (e.g. Y. Bhargava et al. 2019, 2023).

Jointly with X-ray observations, UVIT observed the source with four FUV filters consecutively, in order: *F*148*W* (CaF2-1), *F*154*W*

[3]https://irsa.ipac.caltech.edu/Missions/2mass.html
[4]https://astrobrowse.issdc.gov.in/astro_archive/archive/Home.jsp
[5]http://astrosat-ssc.iucaa.in/uploads/laxpc/LAXPCsoftware22Aug15.zip

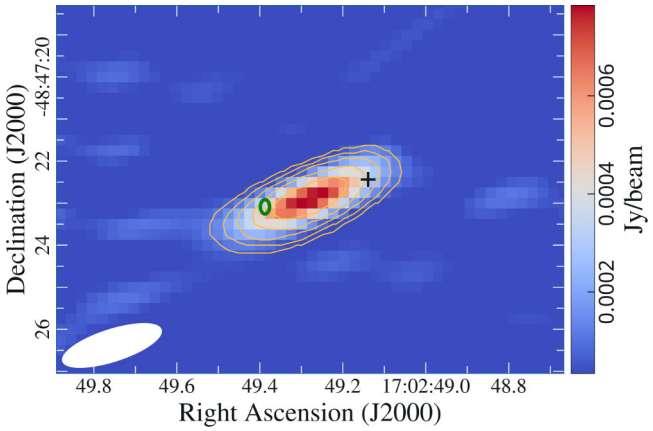

Figure 2. Radio image of GX 339–4 taken on 2024 March 10 at 9 GHz. The green oval denotes the optical *Gaia* position of GX 339–4, with the size of the ellipse equal to the uncertainty on that position. Radio contours are $\sqrt{2}^n$ times the image r.m.s. (25 μJy beam^{-1}) and n = 5,6,7,8.... The colour bar on the right gives the flux density. The beam is shown in the lower left of the image. The black cross marks the position of the resolved jet knot from G. Mastroserio et al. (2025), taken ∼2 months later. There is a shift in the radio centroid when compared to the optical position. The detected radio source is thus a downstream jet knot, likely from an ejection event near the hard→soft state transition.

(BaF2), *F*169*M* (Sapphire), and *F*172*M* (Silica); see S. N. Tandon et al. (2020) for filter details. The level 2 processed data were downloaded from AstroBrowse and images from each filter were inspected to identify if the source was detected. Due to a minor pointing offset between UVIT and SXT (which was the primary instrument for the observation as required by the FW mode constraint), we verified the astrometric correction and determined the expected source location using *GALEX* imaging (D. C. Martin et al. 2005). The source was not detected in any of the filters and therefore we placed upper limits in the UV bands, which are fully consistent with our broad-band modelling discussed below.

2.2.7 *ATCA*

The Australia Telescope Compact Array (ATCA) observed GX 339–4 between 2024 March 10 12:40:40 UT and 16:16:50 UT (starting ∼2 h after the final *JWST* science frame). Data were recorded simultaneously at 5.5 and 9 GHz, with 2 GHz of bandwidth at each central frequency. ATCA was in an extended 6 km configuration, providing an angular resolution of $\lesssim$1 arcsec. We used PKS B1934−638 for bandpass and flux density calibration, and the nearby source J1664−50 for gain calibration. Data were first flagged for radio frequency interference before being calibrated and imaged following standard procedures within the COMMON ASTRONOMY SOFTWARE APPLICATION (CASA v. 5.3; CASA Team 2022). We used a Briggs robust parameter of 0 and fit for a point source in the image plane.

Fig. 2 shows the resultant ATCA image at 9 GHz. The detected radio source does not arise from the core position of GX 339–4; instead the detection is shifted from the optical *Gaia* DR3 position of GX 339–4 (Gaia Collaboration et al. 2016, 2023) to the west by ≈1.2 arcsec, along its known jet axis (e.g. E. Gallo et al. 2004; S. Corbel et al. 2010; G. Mastroserio et al. 2025), implying that we are witnessing emission associated with a jet ejection event – a downstream jet knot likely launched near the hard-to-soft state transition. G. Mastroserio et al. (2025) presented radio observations taken ∼2 months after our *JWST* campaign, finding a discrete jet knot separated from the optical core by 2.6 arcsec along the same direction (marked by the black cross in Fig. 2). These facts suggest a self-consistent scenario whereby the jet knots are the same between the various radio observations, having travelled further by the time of the G. Mastroserio et al. (2025) observations. Assuming an ejection date of Jan 25 when the hard-to-soft transition occurred (45 d prior to our campaign; cf. H. Negoro et al. 2024), our detected offset implies a travel distance of $4.7(\pm0.1)\times10^{-2}$ pc, at an average superluminal speed of $\approx 1.2\,c$. The measured flux densities of the detected knot are 1.36±0.03 mJy at 5.5 GHz and 0.89±0.03 mJy at 9 GHz, respectively, consistent with an optically thin spectral slope from synchrotron-emitting ejecta. Imaging the radio data on shorter time-intervals to explore intra-observational variability, we find the radio flux density to be steadily rising throughout the radio observation.

Due to the presence of this bright ejection, we can only place weak constraints on the brightness of the radio core. Subtracting a point source from the best-fitting position of the ejecta to remove it, we find a 3σ upper limit on the flux density at the core position of 0.25 mJy at 5.5 GHz and 0.15 mJy at 9 GHz. See Section 4.4 for further discussion, and full details of the radio (and subsequent sub-mm) analysis will be presented in Russell et al. (in preparation).

2.2.8 *ALMA*

GX 339–4 was observed with the Atacama Large (Sub-)Millimeter Array (ALMA; Project Code: 2023.A.00018.T) on 2024 March 10 between 10:55 and 11:49 UTC, for a total on-source observation time of ∼17 min. Data were taken in Bands 3, 4, and 6 at central frequencies of 97.5, 145.0, and 233.0 GHz, respectively. The ALMA correlator was set up to yield 4 × 2 GHz wide base-bands, with a 2.0-s correlator dump time. During our observations, the array was in its Cycle 10 C1 configuration with 43 antennas. The median precipitable water vapour ranged from 3.8 to 4.2 mm during the observations. We reduced the data within the CASA v. 6.2 package (J. P. McMullin et al. 2007), using the ALMA pipeline to calibrate the data. We used J1617–5848 as a band-pass/flux calibrator and J1650–5044 as a phase calibrator.

Similar to the ATCA results, we detected a source offset from the known source position of GX 339–4, indicating a jet ejection. To extract flux densities of this source, we performed multifrequency synthesis imaging with the `tclean` task within CASA, using a natural weighting scheme to maximize sensitivity. Flux densities were measured from these images by fitting a point source in the image plane (with the `imfit` task within CASA). We significantly detect the source at 97.5 and 145.0 GHz, with flux densities of 0.35 ± 0.03 and 0.26 ± 0.04 mJy, respectively. At 233.0 GHz, however, we achieve only a non-detection with a 3σ upper limit of 0.18 mJy. We place conservative constraints of <0.15, <0.1, and <0.18 mJy at the core position of GX 339–4 at 97.5, 145, and 233 GHz, respectively.

2.3 Reddening

Reddening to the source is somewhat uncertain, with values spanning $E(B\text{–}V)\approx1.0$–1.2 and corresponding extinctions A_V ≈ 3.0–4.2 mag quoted in the literature (e.g. A. A. Zdziarski et al. 1998, 2019; P. Gandhi et al. 2011b). Estimates based on reddening of field stars (e.g. J. E. Grindlay 1979), on intervening absorption

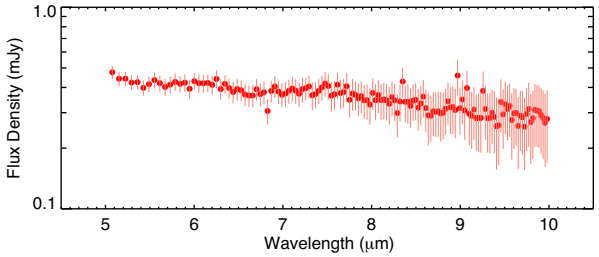

Figure 3. Observed MIRI low-resolution spectrum of GX 339–4 during the 2024 March soft state. The points denote the median across all integrations, and error bars denote the standard deviation incorporating background and instrumental errors together with intrinsic source variability.

components (R. I. Hynes et al. 2004), and from modelling the spectrum of GX 339–4 itself (M. Cadolle Bel et al. 2011; I. A. Kosenkov et al. 2020), are all broadly consistent within uncertainties.

Here, we utilize a nominal extinction value $A_V = 3.5$ mag, but with an uncertainty of $\Delta A_V = 0.5$ mag propagated through all corrections necessary for model fitting, assuming a normal distribution. The extinction curve wavelength dependence follows the widely adopted J. A. Cardelli, G. C. Clayton & J. S. Mathis (1989) law over the ultraviolet to optical range, and this is extended to the MIR using the recommended interstellar extinction from J. E. Chiar & A. G. G. M. Tielens (2006). Dereddening is most important for the optical–UV regime. In the MIRI range, the flux correction factors for GX 339–4 are much milder, with an average value of 1.2, and peaking around 1.4 near 10 μm. The adopted extinction curve is also tabulated in the Appendix B for reference, and a tabulated version of the broad-band data corrected for absorption can be found in Appendix C.

One caveat to note is that the inferred gas column density that we derive later from the X-ray analysis ($N_H \approx 7 \times 10^{21}$ cm^{-2}; see Section 3.2) suggests somewhat smaller optical extinction of $A_V \approx 2.4$ mag using recent gas-to-dust absorption-to-extinction conversion relations (e.g. A. Bahramian et al. 2015; D. R. Foight et al. 2016). This would not reduce the accretion disc reprocessing inferred in the optical, but would not impact the MIR corrections significantly.

3 RESULTS

3.1 MIRI spectral-timing

GX 339–4 is detected with MIRI at flux densities spanning 0.5–0.3 mJy across the wavelength range of 5–10 μm. The median spectrum, shown in Fig. 3, can be characterized by a simple power-law with exponent $\alpha^{\rm obs}_{\rm MIRI} = +0.39 \pm 0.07$ (with flux density $F_\nu \propto \nu^{\alpha^{\rm obs}_{\rm MIRI}}$). The spectrum is featureless to within uncertainties, with no significant emission or absorption features. By artificially injecting emission lines, we estimate a line flux upper limit of $\lesssim 4 \times 10^{-16}$ erg s^{-1} cm^{-2} near $\lambda = 7.5$ μm, the wavelength of the hydrogen Pfund(6–5) emission line – one of the strongest recombination emission lines expected in the MIRI range.

Extracting light curves, the source is found to be significantly variable. Fig. 4 shows this, with the time-series photometry split by wavelength. The observed stochastic variations are qualitatively different to those seen during the hard accretion states of the source at other wavelengths – the overall variability is damped w.r.t. the hard state, and there is an absence of obvious strong flares and characteristic quasi-periodicities (cf., P. Gandhi et al. 2010, for comparison). The strength of time-series variability can be characterized by the excess r.m.s. of variability amplitude above statistical noise (cf. S. Vaughan et al. 2003). Utilizing this formalism for different portions of the MIRI spectrum, we find a mean excess r.m.s. value of 0.04–0.05 (4–

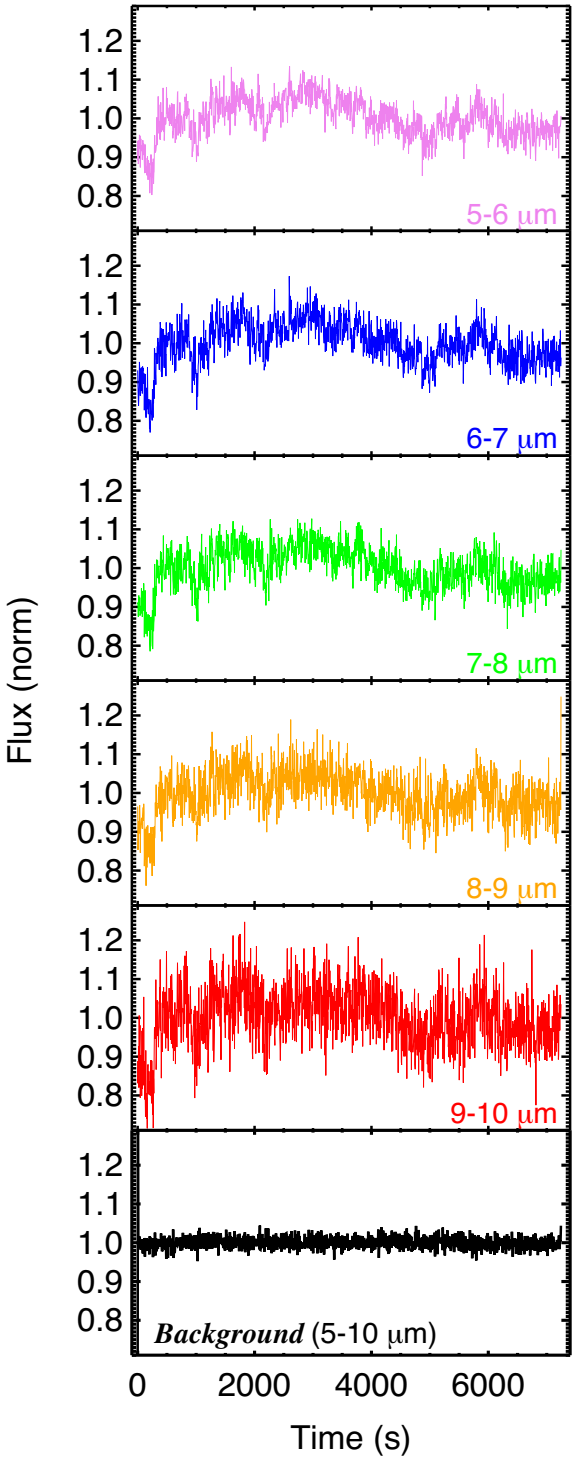

Figure 4. Multiwavelength time-series across all 1400 integrations, split into annotated wavelength bins and normalized to the mean in each case. The bottom panel shows the background level with the same normalization for the full (5–10 μm) band.

5 per cent) across most of the spectral range, as shown in Fig. 5. Bootstrapping the full light curve yields a mean and uncertainty of r.m.s. $= 4.7\,(\pm 0.1) \times 10^{-2}$. Though there appears to be a slight rise towards the red end, we caution that systematic uncertainties in the MIRI pipeline may be underestimating the long-wavelength noise, so this should be treated with caution (see more extensive discussion and appendix in P. Gandhi et al. 2025). Irrespective, the figure shows that the r.m.s. is well above that measured in the background. Also overplotted are the r.m.s. measurements from the bright 2010 hard state as observed by *WISE* in the $W2$ (4.6 μm) and $W3$ (12 μm) filters (P. Gandhi et al. 2011b).[6]

Stochastic variability can be characterized by its Fourier power spectral density (PSD), shown in panel (b) of the same figure for the white-light data as being approximately representative across wavelengths. At high frequencies, the PSD flattens to a constant value, characteristic of white-noise. We fitted the PSD with a combination of a simple power-law–plus–constant as a function of Fourier frequency f, finding an acceptable fit with slope $\beta = -1.58 \pm 0.14$ (Power $P_f \propto f^{\beta}$). To our knowledge, this is the first reported PSD of a transient XRB in the MIR, so comparisons with previous measurements do not exist. In the NIR and red optical filters, however, the hard state PSDs are generally flatter, indicative of fast flickering activity (P. Casella et al. 2010; P. Gandhi et al. 2010; J. A. Paice et al. 2019; F. M. Vincentelli et al. 2019), which is absent here.

The light curves in Fig. 4 show excellent correspondence across all wavelengths. This is confirmed through a cross-correlation function (CCF) analysis, which correlates two light curves as a function of time lag. Panel (c) in Fig. 5 shows high CCF peak values at zero lag, demonstrating the close match between bands with no significant delay. The longer wavelength CCFs are marginally asymmetric, showing a skew to long delays of ≈ 500 s, but this is too subtle to be robustly interpreted without more dedicated analysis, especially given the aforementioned systematic uncertainties and rising statistical noise issues towards the red.

3.2 Broad-band spectral energy distribution

The observed broad-band spectral energy distribution (SED) is shown in Fig. 6. Our collated data span approximately nine orders of magnitude of the electromagnetic spectrum from radio to X-rays, comprising a rich multiwavelength soft-state coverage. The intrinsic continuum is dimmed by reddening and obscuration from the MIR to X-rays. When dereddening the optical to near-IR (ONIR) range using the prescription from Section 2.3, the ONIR slope approximates a simple power law with $\alpha_{\rm ONIR} = +1.80 \pm 0.15$, consistent with the long-wavelength tail of optically thick emission (Fig. 7). Dereddening corrections have only a small impact on the MIRI band, resulting in a corrected slope $\alpha_{\rm MIRI} = +0.36 \pm 0.07$. By contrast, the radio-to-sub-mm power law associated with the extended ejecta is optically thin, with exponent $\alpha_{\rm RS}^{\rm ejecta} = -0.57 \pm 0.03$.

These observations occurred during an X-ray bright soft state, when disc emission is expected to be prominent. G. Mastroserio et al. (2025) have presented such a fit incorporating a Kerr disc, thermal Comptonization, and other narrow features to model the X-ray continuum. Our modelling is qualitatively similar to theirs,

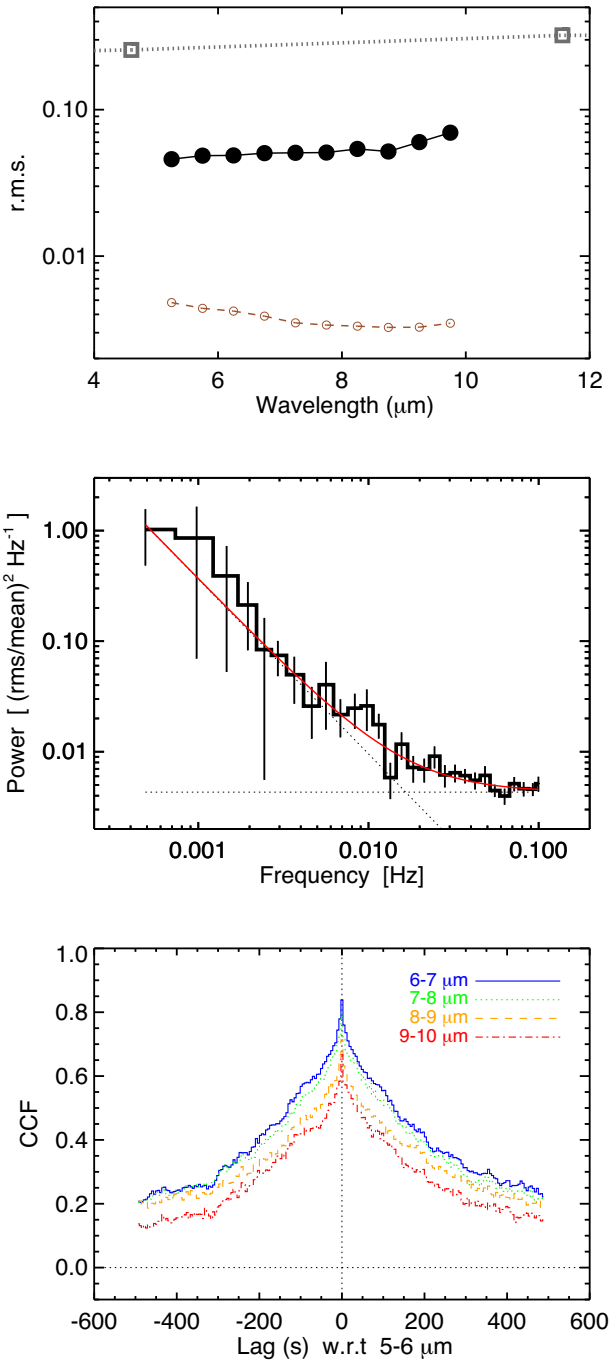

Figure 5. MIRI spectral-timing properties. *(a)* The excess fractional variability r.m.s. of the MIRI data as a function of wavelength (filled black circles), compared to that of the background (empty brown circles with dashed curve) and that of *WISE* hard state observations from 2010 (grey empty squares with dotted lines; P. Gandhi et al. 2011b). The soft-state MIR r.m.s measurement is clearly significant, but substantially weaker than in the hard state. *(b)* The PSD of the white-light time series, with a power law (slope $= -1.58 \pm 0.14$) plus constant fit overplotted (the dotted black lines denote the two model components, and the red solid curve is their sum). *(c)* CCFs between the respective annotated light curves and the shortest wavelength 5–6 μm light curve (used as a baseline reference). The excellent match between the wavelengths is apparent.

[6]Note that *WISE* sampling was far more sparse than MIRI, comprising 13 epochs over a period of ≈ 24 h.

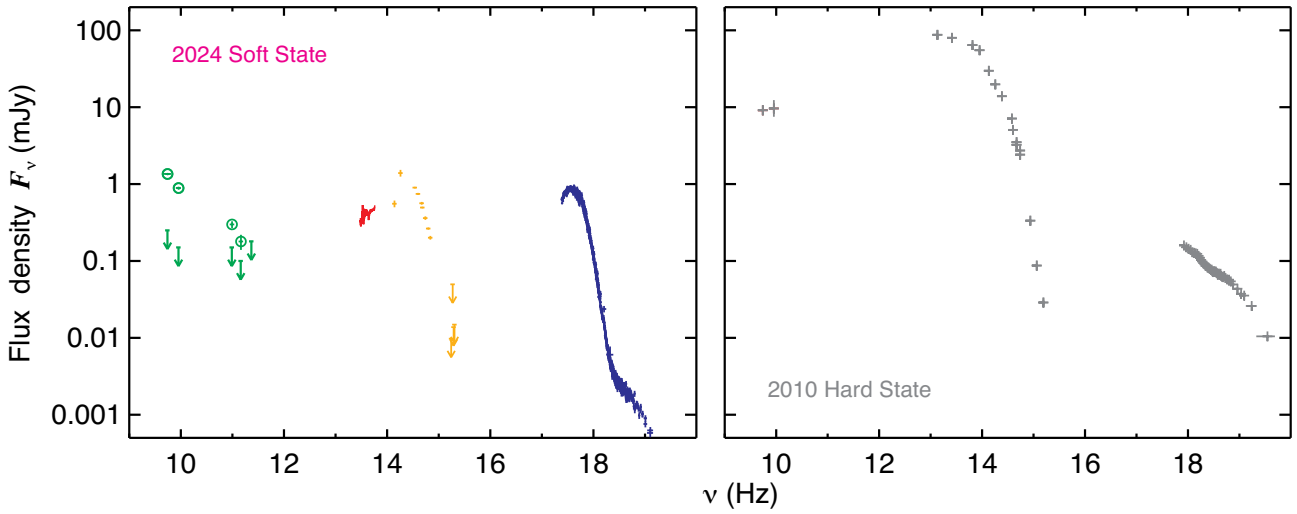

Figure 6. Observed broad-band SED during the 2024 soft state in flux density units (*left*), compared to the hard state 2010 SED in grey (*right*). These plotted flux densities are the observed measurements, not corrected for absorption. X-ray detector spectral responses have been folded out and instrumental cross-calibration removed for display. The instruments used are described in Section 2 and in Appendix A. The unfilled green circles in the radio and sub-mm on the left show the extended ejecta emission, with arrows denoting 3σ upper limits at the core. For full details on the 2010 hard state data shown on the right, we refer the reader to P. Gandhi et al. (2011b).

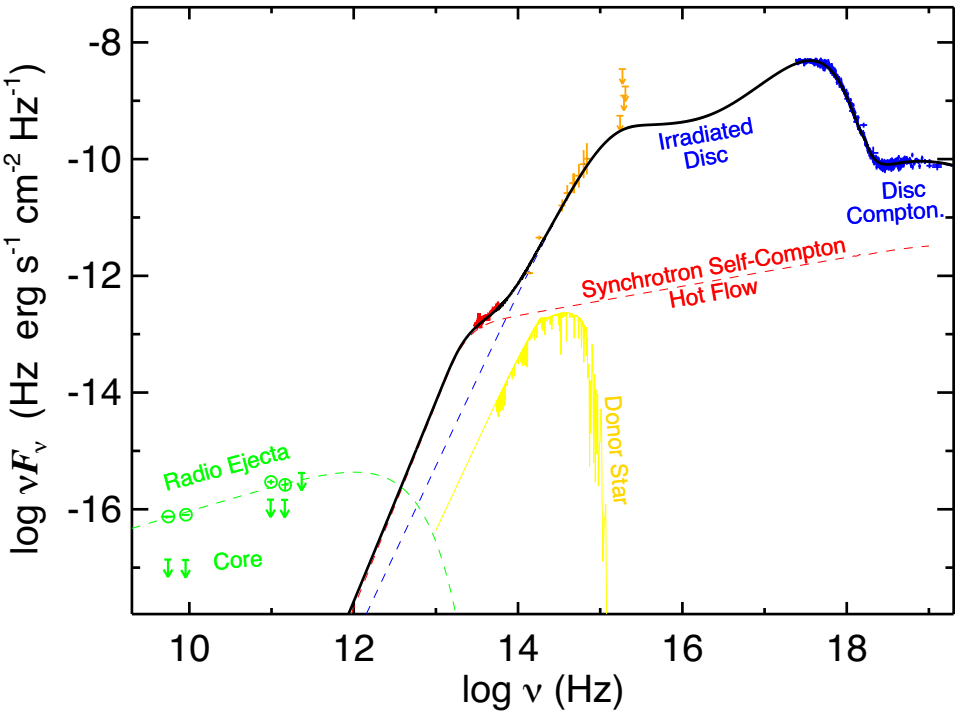

Figure 7. Intrinsic broad-band SED of GX 339–4 in νF_ν units. The primary modelled spectral components are (i) a viscous inner accretion disc and Comptonization in X-rays, (ii) the irradiated outer disc in the optical-to-near-IR, and (iii) a synchrotron-emitting hot flow dominating the MIR. The thick black curve denotes the sum of all the above components. In order to show the intrinsic spectral shape, absorption corrections have been applied to the data and model components where relevant. A K2III spectral template ($T = 4500$ K, $\log g = 2.0$) is also shown in yellow, normalized to the (dereddened) H-band flux density quoted in M. Heida et al. (2017), though this does not dominate any portion of the SED. Finally, a cut-off power law is fitted to the extended radio/sub-mm ejecta detections in green. The corresponding green arrows denote the upper limits to the radio/sub-mm emission at the core.

except that we are here interested in covering the full SED including energies much lower than X-rays alone. We thus attempted a `diskir` model fit, which combines a standard multicolour disc (K. Mitsuda et al. 1984) with a Comptonized high-energy tail that irradiates both the inner and outer disc regions. The irradiated outer disc reprocesses this emission to the OIR, in a manner consistent with its local temperature and the reprocessing fraction (M. Gierliński, C. Done & K. Page 2009). This combi-

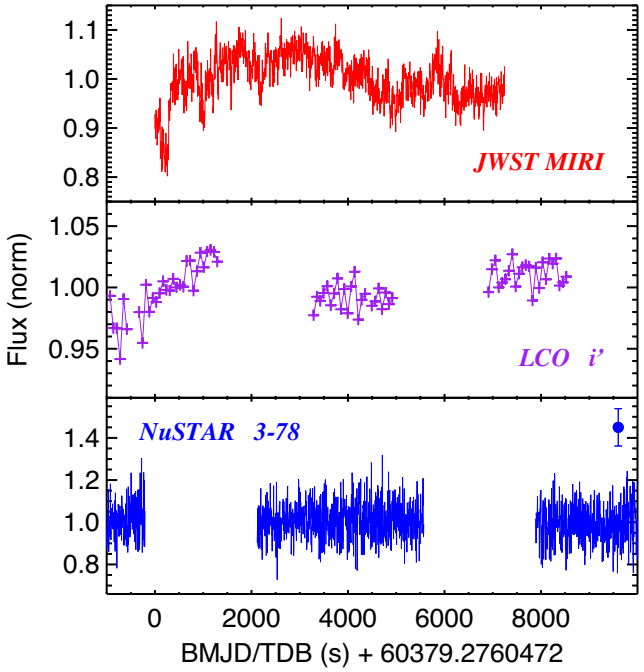

Figure 8. Strictly simultaneous overlap between the time series data sets gathered with *JWST* MIRI (5–10 μm), LCO (i' band), and *NuSTAR* FPMA + B (3–78 keV). Note the different y-axis ranges used across the panels, in order to highlight the variability. Statistical uncertainties are important only for the *NuSTAR* data set in the bottom panel, where a representative error bar is overplotted in the top corner.

nation allows joint modelling of the X-rays and the ONIR regime. The primary fits were conducted in the `xspec` package (K. A. Arnaud 1996), using Levenberg–Marquardt minimization, and quoted confidence ranges for the SED fit are 90 per cent intervals corresponding to $\Delta\ \chi^2 = 2.71$ for one parameter of interest. The fraction $f_{\rm out}$ of the inner disc radiation, which is reprocessed into the OIR, is $f_{\rm out} = 7.9^{+15.8}_{-5.1} \times 10^{-3}$. The outer disc radius ranges over sizes of $10^{4.4-4.6}$ times the inner disc radius. Comptonization of disc photons to higher energies accounts for the weak high-energy X-ray tail seen in *NuSTAR*. The observed (absorbed) X-ray flux of this model fit is $F_{2-10\ \rm keV} = 2.2 \times 10^{-9}$ erg s^{-1} cm^{-2}, with the 10–100 keV hard X-ray flux being 10 times weaker.

The MIRI spectral slope is not consistent with such an irradiated disc, and we will discuss its origin in the following section, along with full model parameters for the combined multiwavelength fit. Here, we simply note that the secondary star is proposed to be of spectral type K2III (M. Heida et al. 2017), with a peak in the ONIR regime, and with only a minor flux contribution to the MIRI band of at most a few per cent.

3.3 Multiwavelength variability

At least two of the data sets with time series measurements in our campaign were able to be coordinated strictly simultaneously with the MIRI observation: *NuSTAR* and LCO in the i' band. The respective light-curve segments spanning the *JWST* window are shown in Fig. 8. X-ray variability is typically suppressed during the soft states of XRB outbursts, and we found an upper limit of only 0.02 to the fractional r.m.s. of the *NuSTAR* light curve.

By contrast, the i' band shows significant fluctuations, with a qualitatively similar trend to that seen in MIRI: there is a rise near

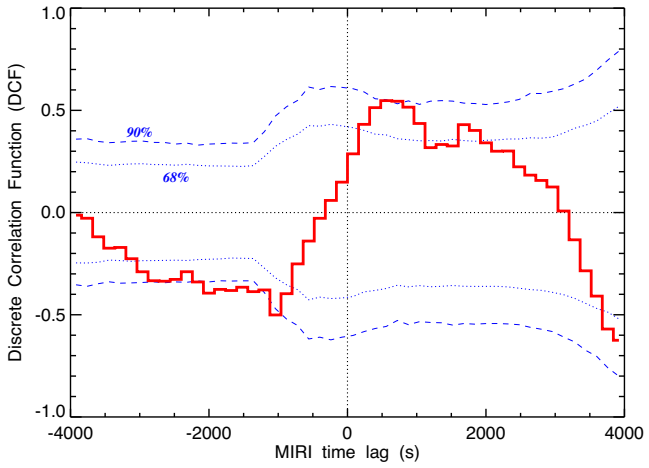

Figure 9. DCF between MIRI and LCO i'. Positive lags denote a time delay of MIRI w.r.t the optical. The blue dotted and dashed contours denote 68 per cent and 90 per cent confidence intervals, respectively, based on 5000 simulated DCFs and power-law noise light curves.

the beginning of the observing window, followed by a fall in the mean level by a few per cent and then a slight rise towards the end again. The i' fractional r.m.s. is measured to be $2.0\,(\pm 0.5) \times 10^{-2}$.

In order to quantify the relationship between the LCO and MIRI bands, we cross-correlate the two light curves. Specifically, we utilize discrete correlation function (DCF) analysis, which measures the degree of linear correlation while allowing for non-uniform time sampling (R. A. Edelson & J. H. Krolik 1988). Both sets of light curves were transformed to the common Solar System Barycentric Dynamical Time (TDB) frame before cross-correlating. We note that LCO timing is GPS-controlled, and the absolute timing accuracy of *JWST* has been validated to be within the demands of lag measurement relevant here (A. W. Shaw et al. 2025).

Fig. 9 shows the DCF result. The peak lag at a few hundred seconds indicates the presence of a time delay with the MIR lagging behind i' by $\approx 750^{+1100}_{-350}$ s, and uncertainties based on bootstrap resampling. As will be discussed in the following sections, this lag is too long to be easily explained by any of the physical scenarios we believe to be relevant in this system. Furthermore, testing for lags using different segments of the data does not yield consistent results on the lag estimate.

The sparse time sampling, particularly in the optical, raises the possibility of a spurious signal arising from chance coincidence amidst stochastic variability. In order to test this hypothesis, we conducted simulation tests of the DCF significance by using randomized light curves. An ensemble of 5000 light curves were created with the red-noise generation algorithm of J. Timmer & M. König (1995) and the MIRI periodogram from Section 3 as a baseline. These light curves match the *statistical* properties of the MIRI data while being completely uncorrelated with our observed data. Thus, the mean DCFs of these randomized MIRI light curves with the LCO data should result in zero mean cross-correlation, and their scatter will be informative of the significance of any particular DCF value. Fig. 9 shows the result of this test as the dotted and dashed contours, representing the 68 per cent and 90 per cent confidence scatter among our 5000 random DCFs. This test demonstrates that DCF values as large as the peak seen in our data *can* arise by coincidence, with our confi-

dence limited to no more than ≈ 90 per cent. Thus, any inference of a lag here should be treated with caution.

Finally, we note that there are two additional simultaneous data sets that require some dedicated analysis and will be presented in follow-up works. The *NICER* camera aboard the International Space Station (Z. Arzoumanian et al. 2014) observed the source at the same time as MIRI (Obs ID 7702010121), but the observation was conducted during orbit *daytime*, and thus requires custom processing to ensure appropriate screening and analysis. In addition, there are HAWK-I NIR *timing* data, which also require dedicated analysis. Both of these will be presented in a follow-up work focused on the multiwavelength timing properties of the source.

4 DISCUSSION

The unabsorbed bolometric luminosity of GX 339–4 during the observed state is dominated by the `diskir` model, $L_{\rm Bol} = 1.2 \times 10^{38}\ (d/8\,{\rm kpc})^2\,{\rm erg\,s^{-1}}$. The corresponding Eddington fraction is $L_{\rm Bol}/L_{\rm Edd} = 0.15\,(d/8\,{\rm kpc})^2\ (M_{\rm BH}/6\,{\rm M_\odot})^{-1}$. These estimates are nearly identical to the source power during the *WISE* observations of the 2010 hard state for the same assumed $M_{\rm BH}$, though the spectrum peaked in higher energy X-rays at that time (P. Gandhi et al. 2011b). The 2010 broad-band SED is overplotted in Fig. 6 in grey. The MIR band fluxes are separated by ≈ 2.5 dex between the two campaigns, a difference larger than in any other portion of the spectrum. Radio fluxes are lower in the 2024 soft state by at least 1 dex, with the monochromatic ejecta luminosity of $\nu L_\nu^{\rm ejecta}\,(5\,{\rm GHz}) = 5.7 \times 10^{29}\,{\rm erg\,s^{-1}}$, and the upper limit on the core being even lower, $\nu L_\nu^{\rm core}\,(5\,{\rm GHz}) < 1.0 \times 10^{29}\,{\rm erg\,s^{-1}}$. Strong quenching of the jet in the soft state can easily account for these changes. Pronounced soft state jet decrements have previously been reported in the radio for 4U 1957–11 (T. J. Maccarone et al. 2020, up to 1500–3300×), MAXI J1535–571 (T. D. Russell et al. 2020), and Swift J1753.5–0127 (A. P. Rushton et al. 2016), among others.

What, then, is the origin of the mid-IR continuum observed by MIRI? There was no detectable core jet activity during our campaign, with the radio and sub-mm detections reflecting residual ejecta emission from earlier in the outburst (Russell et al. in prepation). The MIR slope $\alpha_{\rm MIRI}$ matches neither $\alpha_{\rm ONIR}$ nor $\alpha_{\rm RS}^{\rm ejecta}$, so the MIRI continuum cannot be connected seamlessly at either end. We consider several possible physical scenarios for the original of the MIR emission below.

4.1 Circumbinary disc?

Thermal emission from dust with characteristic temperatures of a few hundred Kelvin contributes copiously to the IR emission of active galaxies. The possibility of dust emission peaking in MIR XRB observations has previously been raised, where it has been attributed to a putative CBD (M. P. Muno & J. Mauerhan 2006). Such discs may be the result of fallback of ejecta from the progenitor supernova, or owe their origin to outflows as part of the accretion–feedback cycle of the compact object. Sensitive observations such as ours, which are not strongly impacted by bright non-thermal jet emission, provide an excellent opportunity to test this scenario.

We included a single-temperature blackbody model in our broad-band SED fit to test for any putative CBD component. Both its temperature and normalization were left free to vary. This was fitted to the broad-band data in conjunction with the absorbed *diskir* component, using `xspec` as before. A simple cut-off power law was additionally included to account for the radio–sub-mm regime; this represents the ejecta emission and does not significantly impact on the IR fit. The complete set of fitted model parameters are listed in Table 2, and the resultant SED is shown in Fig. A2.

An acceptable fit with $T_{\rm CBD} = 748^{+50}_{-46}\,{\rm K}$ was found. The blackbody flux is $2.5 \times 10^{-13}\,{\rm erg\,s^{-1}\,cm^{-2}}$, or $L_{\rm CBD} = 1.9 \times 10^{33} (d/8{\rm kpc})^2\,{\rm erg\,s^{-1}}$, which implies an emitting radius $r_{\rm CBD} = 3 \times 10^{12}\ \sqrt{(4\pi/\Omega)}\,{\rm cm}$, with Ω being the effective solid angle of the emitting CBD surface. For a binary separation $a \approx 12\,{\rm R_\odot}$ this radius corresponds to $3.7 \times\ a$ at minimum. CBDs are subject to tidal disruption which, for a circularized binary with separation a, occurs at a inner radius $r_{\rm CBD} \approx 1.7\,a$ (P. Artymowicz & S. H. Lubow 1994), so the inferred radius is not in conflict with the tidal disruption radius. Stated systematic uncertainties on the binary separation are approximately 10 per cent (A. A. Zdziarski et al. 2019).

At face value, a CBD is an attractive interpretation of the MIRI spectrum. CBDs may encourage accretion on to the central engine (M. P. Muno & J. Mauerhan 2006),[7] so the presence of a CBD could naturally explain the frequent outbursting behaviour of GX 339–4. This cannot, however, easily explain the observed multiwavelength variability. The dynamical time-scale of a CBD can be written as

$$t_{\rm dyn} = 2\pi \sqrt{\frac{r_{\rm CBD}^3}{GM}} \qquad (1)$$
$$\geq 12.3 \left(\frac{r_{\rm CBD}}{3 \times 10^{12}\,{\rm cm}}\right)^{3/2} \left(\frac{7.1\,{\rm M_\odot}}{M_{\rm tot}}\right)^{1/2}\ {\rm d}.$$

Any viscous or other time-scales are expected to be longer still, by factors of $\alpha_{\rm eff}^{-1}$, the effective viscosity parameter. We also note that small solid angles Ω, as expected for CBDs, could easily push $r_{\rm CBD}$ to be much larger still. Thus, we do not expect substantial CBD variability on timespans of a few thousand seconds, as observed in our MIRI light curves. Finally, a combination of an irradiated outer disc and a CBD (say) would be expected to produce a larger i' variability r.m.s than in MIRI – this is opposite to what we observe. Thus, a CBD appears unlikely. Our SED fit can then be converted to an upper limit on the mass of any putative CBD dominating the MIR emission; using identical formalism and assumptions to P. Gandhi et al. (2011a), we find $M_{\rm dust} < 10^{23}\,{\rm g}$, which, for a standard dust:gas ratio, translates to a total (gas) mass $M_{\rm CBD} < 1.0 \times 10^{25}\,{\rm g}$, or $5 \times 10^{-9}\,{\rm M_\odot}$.

4.2 Wind reprocessing?

The presence of MIR winds has been inferred in two other black hole XRBs observed by *JWST*. GRS 1915+105 shows evidence of a prolific, albeit transient, failed wind in its 'X-ray obscured' state (P. Gandhi et al. 2025). In A 0620–00, the presence of a wind has been inferred from the detection of likely bremsstrahlung emission in its quiescent state at an accretion rate which is orders-of-magnitude lower (Z. Zuo et al. 2025).

Equatorial X-ray winds are typical of soft-state outbursts in XRBs (G. Ponti et al. 2012), and GX 339–4 itself is also known

[7] though the devil lies in the details of the source configuration and interactions (cf., R. Valli et al. 2024).

to host a wind in the soft state as inferred from X-ray (J. M. Miller et al. 2004) and optical spectroscopy of the source (A. Ambrifi et al. 2025, building on prior works including R. Soria, K. Wu & H. M. Johnston 1999; K. Wu et al. 2001; F. Rahoui, M. Coriat & J. C. Lee 2014). The characteristics of the MIRI spectrum are, however, not easily ascribable to a wind. Optically thin bremsstrahlung should produce a nearly flat spectral continuum, as seen in GRS 1915+105. For an optically thick constant mass outflow rate, instead, the frequency dependence scales as $\nu^{2/3}$ (A. E. Wright & M. J. Barlow 1975). Our inferred MIRI slope of $\alpha_{\rm MIRI} = +0.36 \pm 0.07$ fits neither of these. Accounting for contaminating emission from the donor star or accretion disc would not help to alleviate this discrepancy. Furthermore, bremsstrahlung would overpredict the observed radio power, unless there is an additional spectral break between the ALMA and *JWST* band.

A wind could also provide an explanation for the long IR lag relative to the optical, *if* this lag is real (cf. discussion and simulation tests in Section 3.3). This is because the recombination time-scale ($t_{\rm rec}$) within a gaseous windy medium can be estimated as

$$t_{\rm rec} \sim 800\ \alpha_{\rm B}^{-1} \left(\frac{n_{\rm H}}{5 \times 10^9\ {\rm cm^{-3}}}\right)^{-1}\ {\rm s}, \quad (2)$$

where $\alpha_{\rm B}$ is the recombination coefficient with a value $\approx 2.5 \times 10^{-13}\ {\rm cm^3\ s^{-1}}$ for temperatures typical of recombining winds (D. E. Osterbrock & G. J. Ferland 2006), and $n_{\rm H}$ is the gas density in the wind medium, a time-scale not dissimilar to the putative long lag.

However, we do not see evidence of recombination emission lines that may be expected from such a wind. In Section 3, a flux limit of $F_{\rm Pf\alpha}^{\rm lim} \lesssim 4 \times 10^{-16}\ {\rm erg\ s^{-1}\ cm^{-2}}$ was placed on the presence of H(6–5) Pf α – among the brightest emission lines in the MIRI regime. Using the H α equivalent width $W = 10.5$ Å reported by A. Ambrifi et al. during the 2021 soft state as a template together with our measured optical SED continuum, we predict a dereddened H α emission-line flux of $F_{\rm H\alpha} \approx 10^{-13}\ {\rm erg\ s^{-1}\ cm^{-2}}$ at the time of the MIRI campaign. This, in turn, predicts an H(6–5) flux at $\lambda = 7.5\,\mu$m of $F_{\rm Pf\alpha}^{\rm pred} \approx 2 \times 10^{-15}\ {\rm erg\ s^{-1}\ cm^{-2}}$ under standard Case B photoionization conditions (D. G. Hummer & P. J. Storey 1987). Continuum uncertainties, including reddening corrections, are approximately a factor of 2. This predicted flux is about a factor of 5 larger than the actual detection limit, arguing against recombination.

One way to circumvent these limitations and allow for an MIR wind is if the H α line were primarily driven by another process (e.g. disc irradiation), with only a small proportion originating in the wind. Another way to 'hide' lines from the wind would be to boost the gas density $n_{\rm H}$ by several orders of magnitude to make the wind optically thick, but this would push its mass-loss rates up unrealistically.[8]

In summary, even if a wind does exist in the soft state of GX 339–4, we do not see any smoking-gun signatures of it in the MIRI band. Future observations should target simultaneous high-resolution ONIR spectroscopy in order to conduct direct searches for wind signatures. There are also two hydrogen recombination edges expected to exist around 5.8 μm ($n = 8$) and 7.4 μm ($n = 9$), which could be searched for with higher S/N spectroscopy.

[8]Related discussions on high mass-loss rates inferred from the MIRI observations of GRS 1915+105 can be found in P. Gandhi et al. (2025).

4.3 Synchrotron from a hot flow overlying the disc?

An alternative means to power the IR emission is via synchrotron emission from the hot electron population in the inner accretion flow also responsible for producing the hard X-rays (e.g. A. Veledina, J. Poutanen & I. Vurm 2013). The same hot flow has previously been considered to subsume the role of a jet base (S. Markoff, M. A. Nowak & J. Wilms 2005), though we do not observe extended/ continuous jet emission typically associated with the hard state here.

Such hot flow models are not generally available for fitting within `xspec`. However, the essential predicted spectral shape of these models is a featureless and relatively flat continuum over a moderate range of wavelengths, breaking at low frequencies when the overall self-absorption optical depth becomes larger than unity. Such a shape can thus mimic spectral breaks inferred from other processes, such as the CBD component from the previous section, which can now be replaced by synchrotron with a self-absorption cut-off at low frequencies. At higher frequencies, this model shows a flat flux density up to some undetectable cooling break swamped underneath the accretion disc emission. Detailed predictions would rely on a far better understanding of the geometry of this emitting medium in the soft state, but toy models can be used to make a feasibility test.

We start by assuming that the hard tail in the X-rays is from disc Comptonization in the hot plasma, and the IR emission arises from synchrotron generated by the same electrons. We can then equate the synchrotron power and that emerging from Comptonization to the respective magnetic and seed photon energy densities $\frac{L_{\rm Sync}}{L_{\rm Compton}} = \frac{U_B}{U_{\rm ph}}$. If we model this coronal medium as a disc with height h and radius $r_{\rm C}$, then $U_{\rm ph}$ will be $\frac{L_{\rm disc}}{\pi r_{\rm C}^2\, c}$, where $L_{\rm disc}$ is the total luminosity of the seed disc photons and c is the speed of light. The value of h cancels, because the volume is linearly proportional to h, as is the time photons spent in the corona. We can then solve this for the magnetic field and find

$$B = \sqrt{\frac{8\,(L_{\rm Sync}/L_{\rm Compton})\,L_{\rm disc}}{r_{\rm C}^2\, c}}. \quad (3)$$

A characteristic size scale of the corona may be estimated from equation (1) of A. Veledina et al. (2013), for photons emitting optically thin synchrotron at $\nu \sim 10^{14}$ Hz and an electron temperature of 300 keV, as fixed for our broad-band fit (Table 2 for the high-energy power-law tail):

$$r_{\rm C}^{\rm min} = 1.5 \times 10^8 \sqrt{\left(\frac{L_{\rm Sync}}{10^{33}\ {\rm erg\ s^{-1}}}\right)\left(\frac{\nu}{10^{14}\ {\rm Hz}}\right)^{-3}\left(\frac{kT_{\rm e}}{300\ {\rm keV}}\right)^{-1}}\ {\rm cm}. \quad (4)$$

Setting $r_{\rm C} = r_{\rm C}^{\rm min}$ and taking $L_{\rm Sync}/L_{\rm Compton} = 10^{-3}$ (an estimate based on the ratio of the hard X-ray flux to the MIR flux), we find that $B \approx 3.4 \times 10^4$ G.

Here, we have assumed that the MIRI band probes synchrotron emission near the self-absorption (SSA) break, as Fig. 7 indicates. An independent estimate of the B field is possible from the position of this break, for which we take $\nu_{\rm SSA} = 10^{14}$ Hz in the formulation presented by A. P. Marscher (1983):

$$B_{\rm SSA} = 3.1 \times 10^4 \left(\frac{b}{3.5}\right)\left(\frac{\nu_{\rm SSA}}{10^{14}\ {\rm Hz}}\right)^5\left(\frac{F_{\nu,\,\rm SSA}}{0.7\ {\rm mJy}}\right)^{-2}\left(\frac{R}{1.5 \times 10^8\ {\rm cm}}\right)^4\ {\rm G} \quad (5)$$

where b is a constant, taken to be 3.5 based upon a typical synchrotron optically thin spectral slope $\alpha = -0.7$ (cf. table 1 of A. P. Marscher 1983). This estimated B field is encouragingly similar to that obtained from energy density arguments (equation 3).

With our inferred size, we can also consider the variability of the system. The viscous time-scale of a thin accretion disc, which is likely powering the corona, is given, from J. Frank, A. King & D. J. Raine (2002), by

$$t_{\rm visc} = 1.6 \times 10^3 \left(\frac{\alpha}{0.3}\right)^{-4/5} \left(\frac{\dot{M}}{10^{18}{\rm g/s}}\right)^{-3/10} \left(\frac{M_{\rm BH}}{6\,{\rm M}_\odot}\right)^{1/4} \left(\frac{r_{\rm C}}{10^8\,{\rm cm}}\right)^{5/4} {\rm s}. \quad (6)$$

This time-scale is of the same order as the characteristic time-scale of MIRI variability. A model SED qualtitatively satisfying these criteria is presented in Fig. 7, with radii extending over $r = (0.1\text{–}1.5) \times 10^8$ cm ($\approx$10–170 gravitational radii $R_{\rm G}$), $B = 3 \times 10^4$ G, with a uniform B field, optical depth $\tau \propto r^{-2}$, and a luminosity matching that in the MIRI band. The plasma Lorentz factor (γ) distribution follows a power-law distribution expected from shock acceleration with $N(\gamma) \propto \gamma^p$ with $p = -2.5$, and a space density at the outer radius of the hot flow of $n_e \approx 10^{15}$ cm^{-3}. This model can thus self-consistently account for both the MIRI timing properties as well as the MIR spectrum.

There are a few caveats to note. First, the model requires the presence of an extended synchrotron emitting medium in the soft state. The same medium is presumably responsible for the Comptonized emission we see in the X-rays and can constitute an extended corona or disc 'atmosphere' sandwiching the accretion disc, as supported by recent polarimetric observations with the *IXPE* mission (e.g. H. Krawczynski et al. 2022; A. Veledina et al. 2023; A. Ingram et al. 2024; J. Podgorný et al. 2024; M. Ewing et al. 2025; G. Mastroserio et al. 2025). In this picture, our results are the first to probe the physical conditions of this medium directly in the IR. Another apparent coincidence for this scenario to work is the requirement for the SSA break to lie in the MIRI band, straddling frequencies very similar to those inferred for the optically thick-to-thin break associated with the hard-state jet base (P. Gandhi et al. 2011b; D. M. Russell et al. 2013), despite dramatic changes in flux and timing properties between the two states (Fig. 6; P. Gandhi et al. 2008; P. Casella et al. 2010). Finally, we note that the compact size scales and high ionization fractions inherent to such a coronal medium cannot accommodate the long MIR lag tentatively identified in Section 3.3 (though the veracity of said lag remains questionable).

We note that a stronger synchrotron contribution to the optical and near-IR regimes has been proposed for MAXI J1828–249 (S. A. Grebenev et al. 2016). For GX 339–4 instead, the MIR band is the only portion of the spectrum where the synchrotron component dominates the broad-band SED (Fig. 7), and we have explored the limits of what the present data allow. Further tests could come from longer time sampling, or probing far-IR wavelengths (a gap in our current coverage between MIRI and ALMA), as we discuss later.

4.4 Episodic compact jet activity in the soft state?

Recent intensive radio and X-ray monitoring campaigns have revealed evidence of transient compact jet reignition episodes in the soft states several XRBs (T. D. Russell et al. 2019; A. K. Hughes et al. 2025; F. Carotenuto et al. 2026). In one of the most recent studies on BHXB MAXI J1348–630, for example, F. Carotenuto et al. (2026) reported that renewed compact jet activity coincided with an excursion to the hard-intermediate state together with a small but significant rise in X-ray variability r.m.s and weak hard X-ray spectral tails. We did not detect significant X-ray variability during our soft-state campaign on GX 339–4, although our observations lacked the X-ray timing sensitivity of NICER available to F. Carotenuto et al.

We do detect a hard X-ray spectral tail (Section 3.2). And the MIRI power-law spectrum (with slope $\alpha_{\rm MIRI} = +0.39 \pm 0.07$), when extended down to the radio and sub-mm regime is fully consistent with the current core radio and sub-mm detection limits, as illustrated in Fig. A2. This raises the question of whether transient compact jet activity could also have occurred during our soft-state observation.

It is impossible to rule out such a model without core radio/sub-mm detections. However, we find that the same power-law model mildly overpredicts the NIR flux by a factor of $\sim$2 when extrapolated to the K_s band (Fig. A2), unless a sharp spectral cut-off occurs in either the compact jet or the irradiated disc components. Furthermore, the observed multiwavelength variability is not immediately consistent with this scenario. In the internal-shock model, the variability characteristics of the compact jet are driven by the seed X-ray seed photons that feed the jet (J. Malzac 2013). Our MIRI characteristic r.m.s amplitude is, instead, much stronger than that observed in X-rays (Section 3.3), though we do not have enough count statistics in the hard tail alone to isolate any coronal variability from that of the disc.

Finally, we note that the possibility of 'dark' jets with low radiative efficiency in the soft state has previously been postulated by S. Drappeau et al. (2017), but with a very different prediction of the radio versus IR spectral shape to that of our soft-state observation, so this does not appear to be a viable alternative either.

In short, the current data are not immediately consistent with jet emission scenarios, though we cannot rule out transient compact jet activity without deeper radio/sub-mm detections. This motivates searches for such detections during future outbursts, together with any power-law signatures bridging wavelengths between the MIRI and sub-mm bands.

4.5 Archival Mid-IR detections of GX 339–4

Fig. 1 shows that GX 339–4 has been observed at several historical epochs with MIR-sensitive facilities. Some of these data sets, especially the *Spitzer* observations, have not been reported in the literature thus far. While attempting to pin down the origin of the MIRI emission, we returned to these historical data sets to see if they could shed further light on our investigations.

Table 3 lists detections of GX 339–4 using all observations from the *Spitzer* Heritage archive. Where fluxes were unavailable, we measured these ourselves from the Level 2 post-BCD mosaic images using aperture photometry and corrections as described in the *Spitzer* analysis handbooks. Systematic uncertainties on the photometry were estimated by varying the sizes and locations of the source and background apertures. The table shows quiescent detections in 2005 and 2014, together with one early detection in the soft state from 2004 (J. A. Tomsick et al. 2004 further classified this as a 'steep power-law' state).

The table shows that the MIR flux density of GX 339–4 always bottoms out around $\approx$0.15–0.2 mJy, to within uncertainties. Quiescent flux measurements are within a factor of $\approx$2 of our soft state detection, though the source undergoes brightening by orders of magnitude during the intervening hard states. Unless this is a coincidence, it requires a source that is stable and unrelated to the standard outer disc, to a hard-state compact jet, as well as to the companion star (cf. Fig. 7).

It is worth checking the immediately surrounding field of GX 339–4 for any contaminants. The nearest (and brightest

Table 3. Newly measured MIR flux densities of GX 339–4 in archival *Spitzer* observations.

Date UTC	Mission/Band	Flux density mJy	State
2004 Aug 20	Spitzer MIPS 24	0.14 ± 0.04*	Soft/Steep power-law state
2005 Sept 04	Spitzer MIPS 24	0.19 ± 0.03	Quiescence
2014 June 08	Spitzer IRAC 3.6	0.22 ± 0.02	Quiescence
2014 June 08	Spitzer IRAC 4.5	0.18 ± 0.03	Quiescence

*Note.**see also initial report by J. A. Tomsick et al. (2004).

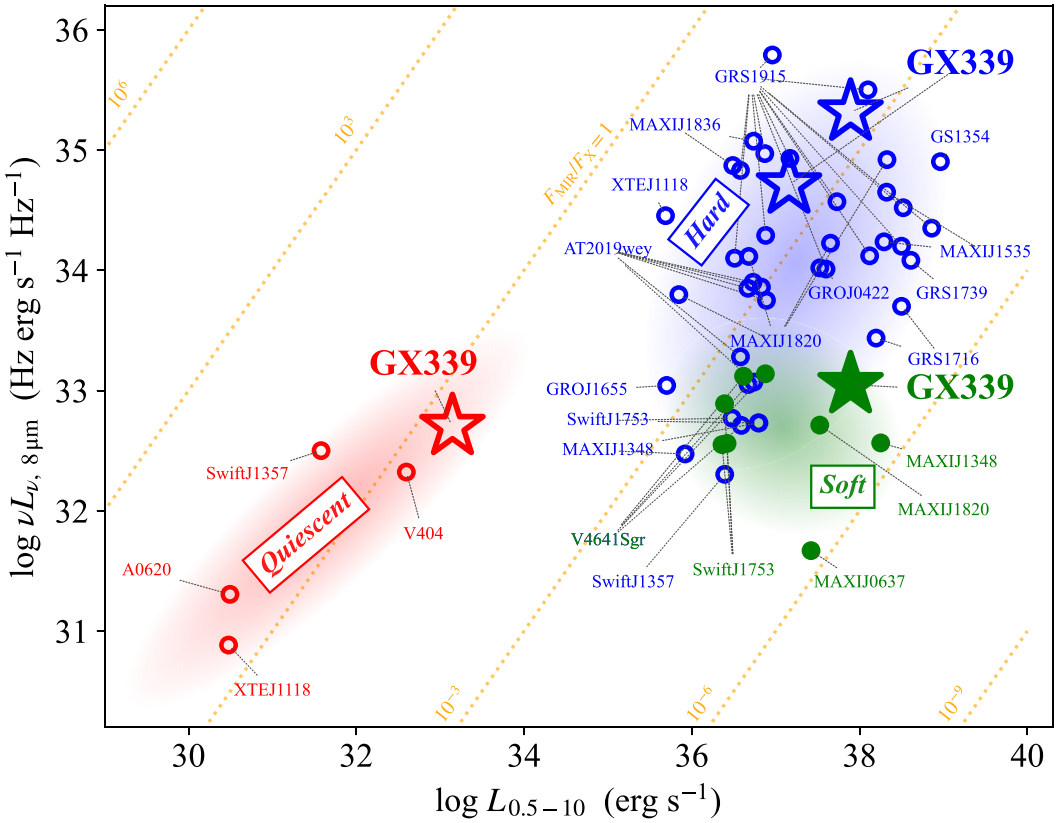

Figure 10. X-ray (0.5–10 keV) versus mid-IR (8 μm) monochromatic luminosity for a sample of MIR-detected black hole XRBs. The red, blue, and green colours are for sources in the quiescent, hard, and soft states, respectively, with GX 339–4 highlighted as a larger star. Lines of constant IR/X-ray flux ratio are denoted in dotted orange. Source names are abbreviated for clarity. The shaded ellipses denote the 2σ covariance regions for the respective states. The plot shows the distinct regimes occupied by sources in the three states. The soft state is typically orders of magnitude more luminous than quiescence in X-rays, whereas in the MIR the contrast between the states is only ~ 1 dex, or even smaller.

within ≈4 arcsec) star is Obj_ID 3 333 279 450 787 716 846 from the Dark Energy Camera Plane Survey (DECaPS2; E. F. Schlafly et al. 2018; A. K. Saydjari et al. 2023), which lies 1.03 arcsec to the north-west of the *Gaia* DR3 optical centroid of GX 339–4, well within the nominal *Spitzer* PSF of ≈ 2 arcsec. The DECaPS2-reported reddest filter (Y-band) flux density is $3.0\,(\pm 0.2) \times 10^{-8}$ Mgy.[9] Assuming a late spectral class (K, say) and similar extinction correction to GX 339–4, this flux density could account for ≈ 0.6 × the *Spitzer* IRAC 3.6 and 4.5 μm quiescent fluxes listed in Table 3. Contaminations fractions reduce steeply to only ≈ 0.1 of the *Spitzer*/MIPS 24 μm band quiescent flux density. These estimates imply that contamination by close neighbours may account for a substantial fraction of the *Spitzer* quiescent fluxes at shorter MIR wavelength but not at the long end. *JWST*'s excellent spatial resolution rules out any contamination to our MIRI extraction.

[9]Maggies (https://www.sdss3.org/dr8/algorithms/magnitudes.php).

4.6 The MIR versus X-ray luminosity parameter space

In Fig. 10, we collate X-ray and MIR detections of transient black hole XRBs in the quiescent, hard, and soft accretion states, in an attempt to identify any underlying trends between these bands. In addition to the analyses presented herein, the data come from archival studies described in Appendix E and Table A3. Other salient details can also be found therein.

Quiescent detections in Fig. 10 are clustered around $F_{\rm MIR}/F_{\rm X-ray} \sim \mathcal{O}(1)$.[10] Hard-state sources show the highest $L_{\rm X-ray}$ and $L_{\rm MIR}$ values. There is a well-known fundamental plane in XRBs coupling the *radio* and X-ray fluxes, and extending from the hard outburst down to quiescence seamlessly for a group of objects on the so-called 'radio-loud' branch, which includes GX 339–4 (e.g. S. Corbel et al. 2003, 2013a; R. M. Plotkin et al. 2012; E. Gallo et al. 2014; E. Tremou et al. 2020). A simple linear regression fit to our quiescent sources with the form

$$\log\left(\frac{\nu L_{\nu,\,8\mu{\rm m}}}{10^{32}\,{\rm erg\,s^{-1}}}\right) = \alpha + \beta\log\left(\frac{L_{0.5-10\,{\rm keV}}}{10^{32}\,{\rm erg\,s^{-1}}}\right) \quad (7)$$

yields the best-fitting parameters of $\alpha = 0.07 \pm 0.19$ and $\beta = 0.53 \pm 0.04$ for the three quiescent and hard state detections of GX 339–4 alone. Interestingly, the slope β matches that obtained when fitting only the quiescent-state sources (for which we find $\alpha = 0.14 \pm 0.20$ and $\beta = 0.59 \pm 0.18$). With the small number of sources included, these fits should be used with some caution. Nevertheless, it is also interesting that these slopes are close to that of the universal radio–X-ray correlation, e.g. the 5 GHz versus 1–10 keV correlation for GX 339–4 presented in E. Gallo et al. 2014 has a slope of 0.62 ± 0.04.

At face value, these similarities would argue for a close connection between the physical processes manifesting the radio and the MIR bands across these two states. However, it is also immediately apparent from the figure that there is a cloud of hard-state detections with enhanced scatter, with many lying at systematically lower MIR luminosities for any given X-ray power. There could be several possible factors at play here, as follows. Our collated sample includes sources that are known to display weak radio jet emission during outburst (e.g. Swift J1753.5–0127, MAXI J1348–630; R. M. Plotkin et al. 2017; F. Carotenuto, S. Corbel & A. Tzioumis 2022), which could result in a corresponding weakness in Fig. 10 if the MIR were also dominated by (inner) jet emission. In some instances, other systematic issues such as distance uncertainties could move their location in the plotted plane (cf. discussion on AT 2019wey, GRS 1716–249 and Swift J1357.2–0933 in Appendix E). Moreover, the cloud of hard-state detections at the luminous end are dominated by GRS 1915+105, which has been in a unique 'X-ray obscured' state for the past few years, and cannot be neatly described as fitting into any of the canonical accretion states (J. M. Miller et al. 2020; P. Gandhi et al. 2025). Finally, unlike the universal jet origin for radio emission, the origin of the MIR is likely to be inherently diverse, e.g. we have inferred the presence of hot flow synchrotron herein for GX 339–4 in the soft state; the quiescent state emission in A 0620–00 is free–free–wind dominated (Z. Zuo et al. 2025), and a jet is thought to drive the flux and variability in V404 Cyg (E. S. Borowski et al. 2025).

The plotted soft state detections are, unsurprisingly, strongly dominated by X-rays, with $F_{\rm MIR}/F_{\rm X-ray} \sim \mathcal{O}(10^{-5})$, and the distribution of our plotted quiescent and soft state sources in MIR–X-ray space is qualitatively similar to that previously seen in fundamental plane correlations in radio–X-ray or NIR–X-ray parameter space (M. Coriat et al. 2009; S. Corbel et al. 2013a). Intriguingly, GX 339–4 lies near the upper end of the distribution of XRBs in all accretion states (soft, hard, and quiescent), approaching or rivalling systems with much larger accretion reservoirs such as V404 Cyg and GRS 1915+105. There is no obvious a priori physical reason for this, and we can only speculate that the inner synchrotron radiation zone (either the hot flow in the soft state, or the compact jet in the hard state) is particularly prominent in GX 339–4. In order to understand the underlying physical conditions driving this, we suggest that detailed studies of the SED and timing properties in quiescence could be enlightening.

There remains much to be unravelled in understanding the location of sources in this MIR–X-ray plane. At minimum, it serves to demonstrate reasonably clear empirical parameter space segregation between the various accretion states, and highlights a progression of high → medium → low $F_{\rm MIR}/F_{\rm X-ray}$ flux ratios, from quiescence → hard → soft state, successively.

Finally, it should be borne in mind that persistent systems are not retained here, and that the 'snapshot' instantaneous measurements included may provide a biased overview of the population. It will thus be important to trace the evolution of individual sources across this diagram through various states, in order to circumvent such biases and to better understand how the strengths of components such as the accretion disc, winds, jet, hot flow synchrotron, and donor star vary across the MIR/X-ray parameter space.

5 SUMMARY

Our core motivation here has been to uncover the physical processes driving the radiative power in accreting black hole systems, and to investigate how these may change with accretion state. GX 339–4 is a prolific multiwavelength transient XRB, and so was a natural target of choice for *JWST* observations.

Our observation window fell on MJD 60379, during (what turned out to be) the declining phase of the 2023/24 outburst. We caught the source in a disc-dominated X-ray state with a clearly detectable high-energy power-law tail (Section 2). The overall source characteristics, including its position in the X-ray HIDs (Fig. 1), a very low X-ray variability r.m.s (Section 3.3), and the disc dominance, are consistent with a fairly typical soft state, despite some uncertainty on the prevalence of the high-energy tail.

We utilized MIRI low-resolution spectroscopy to facilitate IR spectral-timing investigations over the wavelength range of $\approx$ 5–10 μm. A comprehensive multiwavelength campaign was coordinated close in-time with the MIRI observation window. The observations revealed a flat MIR continuum with a flux $\gtrsim 300\times$ fainter than previous hard-state photometric MIR detections (Section 3.2). This can be accounted for by strong suppression of compact jet emission in the soft state, and is supported by the absence of contemporaneous core radio and sub-mm detections (Section 4.4). The MIRI continuum shows significant red-noise variations on time-scales extending to several hundreds of seconds (Section 3.1), which are too short to originate in an extended CBD (Section 4.1). A warm MIR-emitting wind (Section 4.2), on the other hand, cannot easily produce the broad-band spectrum without corresponding recombination emission lines.

The most plausible scenario for powering the observed MIR emission is synchrotron radiation from a coronal hot flow (Section 4.3). With a magnetic field $B \approx 3\times10^4$ G and plasma extended out to $r_{\rm C} \sim 170\,R_{\rm G}$, the same medium could also Comptonize disc photons to account for the high-energy power-law tail, while self-consistently accounting for the MIRI timing properties. In this scenario, the MIR provides a new probe of physical conditions in the coronal hot medium overlaying the disc in the soft

[10] Correcting for partial near-neighbour contamination as detailed in Section 4.5 does not substantially affect the inferences herein.

state, which presumably subsumes the role of an accretion disc 'atmosphere' and the base of the hard-state extended jet. Transient compact jet reignition has been observed in other sources during the soft state; we cannot rule this out without deep core detections, but such a scenario is not easily consistent with the broad-band SED and variability characteristics (Section 4.4).

There is weak evidence of a curiously long time lag between optical and MIR, with the latter lagging the former by several hundred seconds (Section 3.3). A lag of this magnitude would be impossible to reproduce by a hot flow, but simulated significance tests suggest that the inferred lag is instead likely to be a false positive, caused by sparseness in time sampling of the data. The hot flow scenario also requires the synchrotron self-absorption break frequency to remain approximately unchanged between the soft state and the peak of the (far-more MIR-luminous) hard state. This remains puzzling, but could simply be a coincidence. Given these caveats, such a scenario remains to be validated, though encouragingly, the presence of similarly extended coronae has recently been inferred in other XRB X-ray polarization studies. Observations at the redder end (e.g. with MIRI/MRS extending to $\approx 30\,\mu$m) will help to better quantify the underlying spectral slope, any long-wavelength time variability, and also aid in testing competing physical models of a wind, a CBD or soft-state jet activity.

To our knowledge, these are the first reported spectroscopic detections of GX 339–4 in the MIR. Its significant detection – despite the MIR-weak flux level – demonstrates *JWST*'s incredible sensitivity to probe new spectral-timing parameter space. In the process of unravelling the origin of the MIR emission, we analysed and presented several unpublished archival observations of GX 339–4 (Section 4.5) showing that (i) the source's quiescent MIR power lies within a factor of just a few of that seen in the soft state; (ii) in the context of the wider population of black hole transients, GX 339–4 can, at times, be among the most luminous of MIR-emitting XRBs across all accretion states (Section 4.6). With synchrotron (either coronal hot flow or compact jet emission) dominating the soft as well as the hard states, a better understanding of processes driving the quiescent MIR emission will next be important. The MIR–X-ray luminosity plane of black hole transients (Fig. 10) allows isolation of characteristic $F_{\rm MIR}/F_{\rm X-ray}$ flux ratios as a function of accretion state, and enables tracing evolution of the relative fluxes in these two bands as outbursts evolve.

ACKNOWLEDGEMENTS

We are grateful to the mission and instrument teams at STScI for their patience and expert help with our numerous queries, especially MIRI scientist S. Kendrew and staff astronomers I. Wong and G. Sloan. We also thank the anonymous reviewer for suggestions that helped to substantially improve our manuscript.

PG acknowledges funding from The Royal Society (SRF\R1\241074). PG, CDB, and CK thank UKRI Science & Technology Facilities Council for support. AJT, EC, GRS, and COH acknowledge the support of the Natural Sciences and Engineering Research Council of Canada (NSERC Discovery Grants: RGPIN-2024-04458, RGPIN-2021-0400, and RGPIN-2023-04264). AJT additionally acknowledges that this research was undertaken thanks to funding from the Canada Research Chairs Program. TJM acknowledges support from JWST-GO-01586.002. AWS acknowledges support from 80NSSC24K0345 and 80NSSC24K1257. RIH and ESB acknowledge support from JWST-GO-01586.007. JAT acknowledges support from JWST-GO-01586.010-A. TS and FMV acknowledge financial support from the Spanish Ministry of Science, Innovation and Universities (MICIU) under grants PID2020-114822GB-I00 and PID2023-151588NB-I00. JAP acknowledges support from STFC consolidated grant ST/X001075/1. DP acknowledges the support from ISRO (India), under the ISRO RESPOND program. The work of MER was carried out at the Jet Propulsion Laboratory, California Institute of Technology, under a contract with the National Aeronautics and Space Administration. MCB and TDR acknowledge support from the INAF-Astrofit fellowship. DMR, PS, KA, and SKR are supported by Tamkeen under the NYU Abu Dhabi Research Institute grant CASS. SM is supported by a European Research Council (ERC) Synergy Grant 'BlackHolistic' grant No. 10107164. Partial support for KL's effort on the project was provided by NASA through grant numbers HST-GO-16489 and HST-GO-16659 and from the Space Telescope Science Institute, which is operated by AURA, Inc., under NASA contract NAS 5-26555. FMV is supported by the European Union's Horizon Europe research and innovation programme with the Marie Skłodowska-Curie grant agreement No. 101149685. We thank Dan Bramich for his contributions to the development of the XB-NEWS pipeline that processed the LCO data. GM acknowledges financial support from the European Union's Horizon Europe research and innovation program under the Marie Skłodowska-Curie grant agreement No. 101107057 and support from the PRIN MUR SEAWIND (2022Y2T94C), funded by the European Union – Next Generation EU, Mission 4 Component 1 CUP C53D23001330006. PG thanks J. Malzac for discussion regarding the possibility of dark jets in the system, and is grateful to A. Veledina for discussions on the hot flow model.

This work is based on observations made with the NASA/ESA/CSA *James Webb Space Telescope*. The data were obtained from the Mikulski Archive for Space Telescopes at the Space Telescope Science Institute, which is operated by the Association of Universities for Research in Astronomy, Inc., under NASA contract NAS 5-03127 for *JWST*. These observations are associated with program #1586 (P. Gandhi et al. 2021). Support for program #1586 was provided by NASA through a grant from the Space Telescope Science Institute, which is operated by the Association of Universities for Research in Astronomy, Inc., under NASA contract NAS 5-03127. This paper makes use of the following ALMA data: ADS/JAO.ALMA#2023.A.00018.T. ALMA is a partnership of ESO (representing its member states), NSF (USA) and NINS (Japan), together with NRC (Canada), NSTC and ASIAA (Taiwan), and KASI (Republic of Korea), in cooperation with the Republic of Chile. The Joint ALMA Observatory is operated by ESO, AUI/NRAO, and NAOJ. The National Radio Astronomy Observatory is a facility of the National Science Foundation operated under cooperative agreement by Associated Universities, Inc. We thank the ALMA director for granting our DDT request, used to obtain the ALMA mm data analysed in this paper.

This research has made use of the NASA/IPAC Infrared Science Archive, which is funded by the National Aeronautics and Space Administration and operated by the California Institute of Technology. The DOI of the *Spitzer* Enhanced IRS Products is 10.26131/IRSA399.

This research has made use of MAXI data provided by RIKEN, JAXA, and the MAXI team.

This publication uses the data from the *AstroSat* mission of the Indian Space Research Organisation (ISRO), archived at the Indian Space Science Data Centre (ISSDC). This publication uses UVIT data processed by the payload operations centre at the Indian Institute of Astrophysics.

This research has made use of data and/or software provided by the High Energy Astrophysics Science Archive Research Center (HEASARC), which is a service of the Astrophysics Science Division at NASA/GSFC.

Based on observations with ISO, an ESA project with instruments funded by ESA Member States (especially the PI countries: France, Germany, the Netherlands, and the United Kingdom) and with the participation of ISAS and NASA.

SMARTNet (M. J. Middleton et al. 2017) helped to coordinate observations. We have made use of software and web tools from the High Energy Astrophysics Science Archive Research Center (HEASARC) and made use of data and the 'Build XRT Products' tool supplied by the UK Swift Science Data Centre at the University of Leicester.

DATA AVAILABILITY

The data analysed herein are all publicly available in online telescope archives or can be made available upon reasonable request to the authors. The *JWST* data can be identified using the Program identifier 1586 (DOI: 10.17909/3a3q-fd34).

REFERENCES

Agrawal P. C. et al., 2017, JA&A, 38, 30
Alabarta K. et al., 2024, Astron. Telegram, 16460, 1
Ambrifi A. et al., 2025, A&A, 694, A109
Antia H. M. et al., 2021, JA&A, 42, 32
Arnaud K. A., 1996, in Jacoby G. H., Barnes J. eds, ASP Conf. Ser. Vol. 101, Astronomical Data Analysis Software and Systems V. Astron. Soc. Pac., San Francisco, p. 17
Artymowicz P., Lubow S. H., 1994, ApJ, 421, 651
Arzoumanian Z. et al., 2014, in Takahashi T., den Herder J.-W. A., Bautz M. eds, Proc. SPIE Conf. Ser. Vol. 9144, Space Telescopes and Instrumentation 2014: Ultraviolet to Gamma Ray. SPIE, Bellingham, p. 914420
Baglio M. C. et al., 2018, ApJ, 867, 114
Bahramian A., Heinke C. O., Degenaar N., Chomiuk L., Wijnands R., Strader J., Ho W. C. G., Pooley D., 2015, MNRAS, 452, 3475
Banerjee S. et al., 2024, ApJ, 964, 189
Belloni T., Homan J., Casella P., van der Klis M., Nespoli E., Lewin W. H. G., Miller J. M., Méndez M., 2005, A&A, 440, 207
Bhargava Y., Belloni T., Bhattacharya D., Misra R., 2019, MNRAS, 488, 720
Bhargava Y., Bhattacharyya S., Homan J., Pahari M., 2023, ApJ, 955, 102
Blandford R. D., Königl A., 1979, ApJ, 232, 34
Borowski E. S. et al., 2025, ApJ, 991, L31
Bramich D. M., Freudling W., 2012, MNRAS, 424, 1584
Bright J. S. et al., 2025, MNRAS, 541, 1851
Brocksopp C., Bandyopadhyay R. M., Fender R. P., 2004, New Astron., 9, 249
Burrows D. N. et al., 2005, Space Sci. Rev., 120, 165
CASA Team, 2022, PASP, 134, 114501
Cadolle Bel M. et al., 2011, A&A, 534, A119
Campana S., Colpi M., Mereghetti S., Stella L., Tavani M., 1998, A&AR, 8, 279
Cao H.-M. et al., 2022, A&A, 657, A104
Cardelli J. A., Clayton G. C., Mathis J. S., 1989, ApJ, 345, 245
Carotenuto F., Corbel S., Tzioumis A., 2022, MNRAS, 517, L21
Carotenuto F., Zhang L., Altamirano D., Casella P., Corbel S., Miller-Jones J. C. A., 2026, A&A, 707, A151
Casares J. et al., 2023, MNRAS, 526, 5209
Casella P. et al., 2010, MNRAS, 404, L21
Charles P., Matthews J. H., Buckley D. A. H., Gandhi P., Kotze E., Paice J., 2019, MNRAS, 489, L47
Chiar J. E., Tielens A. G. G. M., 2006, ApJ, 637, 774
Corbel S., Fender R. P., 2002, ApJ, 573, L35
Corbel S., Nowak M. A., Fender R. P., Tzioumis A. K., Markoff S., 2003, A&A, 400, 1007
Corbel S. et al., 2010, Astron. Telegram, 2745, 1
Corbel S., Coriat M., Brocksopp C., Tzioumis A. K., Fender R. P., Tomsick J. A., Buxton M. M., Bailyn C. D., 2013a, MNRAS, 428, 2500
Corbel S. et al., 2013b, MNRAS, 431, L107
Coriat M., Corbel S., Buxton M. M., Bailyn C. D., Tomsick J. A., Körding E., Kalemci E., 2009, MNRAS, 400, 123
Corral-Santana J. M., Casares J., Muñoz-Darias T., Bauer F. E., Martínez-Pais I. G., Russell D. M., 2016, A&A, 587, A61
Done C., Gierliński M., Kubota A., 2007, A&AR, 15, 1
Drappeau S. et al., 2017, MNRAS, 466, 4272
Dunn R. J. H., Fender R. P., Körding E. G., Cabanac C., Belloni T., 2008, MNRAS, 387, 545
Dunn R. J. H., Fender R. P., Körding E. G., Belloni T., Cabanac C., 2010, MNRAS, 403, 61
Dyrek A., Ducrot E., Lagage P. O., Tremblin P., Kendrew S., Bouwman J., Bouffet R., 2024, A&A, 683, A212
Echiburú-Trujillo C. et al., 2024, ApJ, 962, 116
Edelson R. A., Krolik J. H., 1988, ApJ, 333, 646
Evans P. A. et al., 2009, MNRAS, 397, 1177
Ewing M. et al., 2025, MNRAS, 541, 1774
Fender R. P., Belloni T. M., Gallo E., 2004, MNRAS, 355, 1105
Foight D. R., Güver T., Özel F., Slane P. O., 2016, ApJ, 826, 66
Frank J., King A., Raine D. J., 2002, Accretion Power in Astrophysics: Third Edition. Cambridge Univ. Press, Cambridge
Fuchs Y., Mirabel I. F., Claret A., 2003, A&A, 404, 1011
Fuchs Y., Koch Miramond L., Ábrahám P., 2006, A&A, 445, 1041
Gaia Collaboration, 2016, A&A, 595, A1
Gaia Collaboration, 2023, A&A, 674, A1
Gallo E., Corbel S., Fender R. P., Maccarone T. J., Tzioumis A. K., 2004, MNRAS, 347, L52
Gallo E., Migliari S., Markoff S., Tomsick J. A., Bailyn C. D., Berta S., Fender R., Miller-Jones J. C. A., 2007, ApJ, 670, 600
Gallo E. et al., 2014, MNRAS, 445, 290
Gandhi P. et al., 2008, MNRAS, 390, L29
Gandhi P. et al., 2010, MNRAS, 407, 2166
Gandhi P., Isobe N., Birkinshaw M., Worrall D. M., Sakon I., Iwasawa K., Bamba A., 2011a, PASJ, 63, 505
Gandhi P. et al., 2011b, ApJ, 740, L13
Gandhi P. et al., 2016, MNRAS, 459, 554
Gandhi P. et al., 2017, Nat. Astron., 1, 859
Gandhi P. et al., 2021, Black Hole Jet Launching Physics with MIRI , JWST Proposal. Cycle 1, ID. #1586
Gandhi P. et al., 2025, MNRAS, 537, 1385
Gehrels N. et al., 2004, ApJ, 611, 1005
Gierliński M., Done C., Page K., 2009, MNRAS, 392, 1106
Goodwin A. J. et al., 2020, MNRAS, 498, 3429
Grebenev S. A., Prosvetov A. V., Burenin R. A., Krivonos R. A., Mescheryakov A. V., 2016, Astron. Lett., 42, 69
Grindlay J. E., 1979, ApJ, 232, L33
Harrison F. A. et al., 2013, ApJ, 770, 103
Harrison T. E., Gelino D. M., Buxton M., Fost T., 2014, AJ, 148, 22
Heida M., Jonker P. G., Torres M. A. P., Chiavassa A., 2017, ApJ, 846, 132
Heinke C. O., Grindlay J. E., Lugger P. M., Cohn H. N., Edmonds P. D., Lloyd D. A., Cool A. M., 2003, ApJ, 598, 501
Hughes A. K. et al., 2025, ApJ, 988, 109
Hummer D. G., Storey P. J., 1987, MNRAS, 224, 801
Hynes R. I., Steeghs D., Casares J., Charles P. A., O'Brien K., 2003, ApJ, 583, L95

Hynes R. I., Steeghs D., Casares J., Charles P. A., O'Brien K., 2004, ApJ, 609, 317
Ingram A. et al., 2024, ApJ, 968, 76
John C., De K., Lucchini M., Behar E., Kara E., MacLeod M., Panagiotou C., Wang J., 2024, MNRAS, 535, 2633
Kaper L., Trams N. R., Barr P., van Loon J. T., Waters L. B. F. M., 1998, Ap&SS, 255, 199
Kendrew S. et al., 2015, PASP, 127, 623
Kosenkov I. A., Veledina A., Suleimanov V. F., Poutanen J., 2020, A&A, 638, A127
Krawczynski H. et al., 2022, Science, 378, 650
Lasota J. P., 2000, A&A, 360, 575
Lewis F., 2018, Robotic Telescope, Student Research and Education Proceedings, 1, 237 Fitzgerald, M., James, C.R., Buxner, S., White, S., Eds.
Lewis F., Russell D. M., Fender R., Roche P., Clark J. S., 2009, in Proceedings of VII Microquasar Workshop: Microquasars and Beyond – PoS(MQW7). p. 069
Maccarone T. J., Osler A., Miller-Jones J. C. A., Atri P., Russell D. M., Meier D. L., McHardy I. M., Longa-Peña P. A., 2020, MNRAS, 498, L40
Mainzer A. et al., 2011, ApJ, 731, 53
Makishima K., Maejima Y., Mitsuda K., Bradt H. V., Remillard R. A., Tuohy I. R., Hoshi R., Nakagawa M., 1986, ApJ, 308, 635
Malzac J., 2013, MNRAS, 429, L20
Malzac J., 2014, MNRAS, 443, 299
Markoff S., Falcke H., Fender R., 2001, A&A, 372, L25
Markoff S., Nowak M. A., Wilms J., 2005, ApJ, 635, 1203
Marscher A. P., 1983, ApJ, 264, 296
Martin D. C. et al., 2005, ApJ, 619, L1
Mastroserio G. et al., 2025, ApJ, 978, L19
Matsuoka M. et al., 2009, PASJ, 61, 999
McMullin J. P., Waters B., Schiebel D., Young W., Golap K., 2007, in Shaw R. A., Hill F., Bell D. J. eds, ASP Conf. Ser. Vol. 376, Astronomical Data Analysis Software and Systems XVI. Astron. Soc. Pac., San Francisco, p. 127
Middleton M. J. et al., 2017, New Astron. Rev., 79, 26
Migliari S., Tomsick J. A., Maccarone T. J., Gallo E., Fender R. P., Nelemans G., Russell D. M., 2006, ApJ, 643, L41
Migliari S. et al., 2007, ApJ, 670, 610
Miller J. M. et al., 2004, ApJ, 601, 450
Miller J. M. et al., 2020, ApJ, 904, 30
Mirabel I. F., Claret A., Cesarsky C. J., Boulade O., Cesarsky D. A., 1996, A&A, 315, L113
Misra R., Roy J., Yadav J. S., 2021, JA&A, 42, 55
Mitsuda K. et al., 1984, PASJ, 36, 741
Muno M. P., Mauerhan J., 2006, ApJ, 648, L135
Negoro H. et al., 2024, Astron. Telegram, 16424, 1
Osterbrock D. E., Ferland G. J., 2006, Astrophysics of Gaseous Nebulae and Active Galactic Nuclei. University Science Books Sausalito CA
Paice J. A. et al., 2019, MNRAS, 490, L62
Pirard J.-F. et al., 2004, in Moorwood A. F. M., Iye M. eds, Proc. SPIE Conf. Ser. Vol. 5492, Ground-Based Instrumentation for Astronomy. SPIE, Bellingham, p. 1763
Plotkin R. M., Markoff S., Kelly B. C., Körding E., Anderson S. F., 2012, MNRAS, 419, 267
Plotkin R. M. et al., 2016, MNRAS, 456, 2707
Plotkin R. M. et al., 2017, ApJ, 848, 92
Podgorný J. et al., 2024, A&A, 686, L12
Ponti G., Fender R. P., Begelman M. C., Dunn R. J. H., Neilsen J., Coriat M., 2012, MNRAS, 422, L11
Rahoui F., Chaty S., Rodriguez J., Fuchs Y., Mirabel I. F., Pooley G. G., 2010, ApJ, 715, 1191
Rahoui F., Lee J. C., Heinz S., Hines D. C., Pottschmidt K., Wilms J., Grinberg V., 2011, ApJ, 736, 63
Rahoui F., Coriat M., Lee J. C., 2014, MNRAS, 442, 1610
Ressler M. E. et al., 2015, PASP, 127, 675
Rieke G. H. et al., 2015, PASP, 127, 584
Rushton A. P. et al., 2016, MNRAS, 463, 628
Russell D. M., Fender R. P., Hynes R. I., Brocksopp C., Homan J., Jonker P. G., Buxton M. M., 2006, MNRAS, 371, 1334
Russell D. M., Altamirano D., Lewis F., Roche P., Markwardt C. B., Fender R. P., 2008, Astron. Telegram, 1586, 1
Russell D. M., Miller-Jones J. C. A., Maccarone T. J., Yang Y. J., Fender R. P., Lewis F., 2011, ApJ, 739, L19
Russell D. M. et al., 2013, MNRAS, 429, 815
Russell D. M. et al., 2013b, ApJ, 768, L35
Russell D. M., Qasim A. A., Bernardini F., Plotkin R. M., Lewis F., Koljonen K. I. I., Yang Y.-J., 2018, ApJ, 852, 90
Russell D. M. et al., 2019, Astron. Nachr., 340, 278
Russell D. M., Casella P., Kalemci E., Vahdat Motlagh A., Saikia P., Pirbhoy S. F., Maitra D., 2020, MNRAS, 495, 182
Russell D. M. et al., 2022, Astron. Telegram, 15596, 1
Russell T. D., Soria R., Miller-Jones J. C. A., Curran P. A., Markoff S., Russell D. M., Sivakoff G. R., 2014, MNRAS, 439, 1390
Russell T. D. et al., 2019, ApJ, 883, 198
Russell T. D. et al., 2020, MNRAS, 498, 5772
Saikia P. et al., 2022, ApJ, 932, 38
Saydjari A. K. et al., 2023, ApJS, 264, 28
Schlafly E. F. et al., 2018, ApJS, 234, 39
Servillat M., Coleiro A., Chaty S., Rahoui F., Zurita Heras J. A., 2014, ApJ, 797, 114
Shaw A. W. et al., 2025, AJ, 169, 21
Singh K. P. et al., 2014, in Takahashi T., den Herder J.-W. A., Bautz M. eds, Proc. SPIE Conf. Ser. Vol. 9144, Space Telescopes and Instrumentation 2014: Ultraviolet to Gamma Ray. SPIE, Bellingham, p. 91441S
Singh K. P. et al., 2017, JA&A, 38, 29
Skrutskie M. F. et al., 2006, AJ, 131, 1163
Smith H. A., Beall J. H., Swain M. R., 1990, AJ, 99, 273
Soria R., Wu K., Johnston H. M., 1999, MNRAS, 310, 71
Stetson P. B., 1987, PASP, 99, 191
Stetson P. B., 1990, PASP, 102, 932
Tandon S. N. et al., 2017, AJ, 154, 128
Tandon S. N. et al., 2020, AJ, 159, 158
Timmer J., König M., 1995, A&A, 300, 707
Tomsick J. A. et al., 2004, in American Astronomical Society Meeting Abstracts. p. 104.04
Tonry J. L. et al., 2018, ApJ, 867, 105
Tremou E. et al., 2020, MNRAS, 493, L132
Uttley P., Casella P., 2014, Space Sci. Rev., 183, 453
Valli R. et al., 2024, A&A, 688, A128
van Paradijs J., Telesco C. M., Kouveliotou C., Fishman G. J., 1994, ApJ, 429, L19
Vaughan S., Edelson R., Warwick R. S., Uttley P., 2003, MNRAS, 345, 1271
Veledina A., Poutanen J., Vurm I., 2013, MNRAS, 430, 3196
Veledina A. et al., 2023, ApJ, 958, L16
Vincentelli F. M. et al., 2019, ApJ, 887, L19
Vincentelli F. M. et al., 2021, MNRAS, 503, 614
Wachter S., 2008, in Bandyopadhyay R. M., Wachter S., Gelino D., Gelino C. R. eds, AIP Conf. Proc. Vol. 1010, A Population Explosion: The Nature & Evolution of X-ray Binariesin Diverse Environments. Am. Inst. Phys., New York, 210
Wang X., Wang Z., 2014, ApJ, 788, 184
Wright A. E., Barlow M. J., 1975, MNRAS, 170, 41
Wu K., Soria R., Hunstead R. W., Johnston H. M., 2001, MNRAS, 320, 177
Yadav J. S., Agrawal P. C., Antia H. M., Manchanda R. K., Paul B., Misra R., 2017, Curr. Sci., 113, 591
Zdziarski A. A., Poutanen J., Mikolajewska J., Gierlinski M., Ebisawa K., Johnson W. N., 1998, MNRAS, 301, 435
Zdziarski A. A., Ziółkowski J., Mikołajewska J., 2019, MNRAS, 488, 1026
Zhao Y., Gandhi P., Dashwood Brown C., Knigge C., Charles P. A., Maccarone T. J., Nuchvanichakul P., 2023, MNRAS, 525, 1498
Zuo Z. et al., 2025, ApJ, 991, 157

Table A1. Adopted extinction curve for GX 339–4.

λ (μm)	A_λ (mag)	A_λ/A_V
0.148 (CaF2-1)	9.418	2.691
0.154 (BaF2)	9.150	2.614
0.161 (Sapphire)	8.941	2.555
0.172 (Silica)	8.780	2.508
0.436 (B)	4.667	1.333
0.477 (g')	4.236	1.210
0.55 (V)	3.5 ± 0.5	1.0
0.622 (r')	3.016	0.862
0.641 (R)	2.919	0.834
0.754 (i')	2.367	0.676
0.870 (z_s)	1.787	0.510
1	1.414	0.404
1.65 (H)	0.596	0.170
2	0.430	0.123
2.159 (K_s)	0.382	0.109
3	0.248	0.071
4	0.189	0.054
5	0.163	0.047
6	0.151	0.043
7	0.146	0.042
8	0.149	0.043
9	0.272	0.078
10	0.378	0.108
11	0.297	0.085
12	0.234	0.067
13	0.204	0.058
14	0.206	0.059
15	0.217	0.062
16	0.231	0.066
17	0.247	0.071
18	0.263	0.075
19	0.271	0.077
20	0.265	0.076
21	0.250	0.071
22	0.234	0.067
23	0.221	0.063
24	0.207	0.059
25	0.195	0.056
26	0.184	0.053
27	0.174	0.050

APPENDIX A:

Coordination of Multiwavelength Campaign

Once we were informed of the *JWST* observation date and time window, we scheduled multiwavelength observations to coordinate with the *JWST* window. Exact overlap was only possible with other space facilities (e.g. *NuSTAR*), and from Chilean facilities where the observation occurred during local night time. This was further complicated by an unannounced *JWST* window change by a few hours resulting from the failure of a preceding observation.

Despite these issues, all data sets in our final campaign were coordinated to within a few hours of the *JWST* window, all on the same calendar day. The respective observation windows for all facilities are depicted pictorially in Fig. A1. Though times are not aligned to a common timeframe here, any corresponding differences across the observatories are negligible on the plot scale.

Table A2. Tabulated intrinsic (deabsorbed) mean SED for the core of GX 339–4 during our campaign, listed at key frequencies. Upper limits (3σ) are included for non-detections.

Band	Frequency ν log (Hz)	Flux density νF_ν log (Hz erg s^{-1} cm^{-2} Hz^{-1})
ATCA/5.5 GHz	9.74	< -16.86
ATCA/9 GHz	9.95	< -16.87
ALMA/97.5 GHz	10.99	< -15.83
ALMA/145 GHz	11.16	< -15.84
ALMA/233 GHz	11.37	< -15.38
MIRI/10 μm	13.47	-12.84 ± 0.03
MIRI/5 μm	13.78	-12.50 ± 0.03
REM/H	14.26	-11.35 ± 0.04
LCO/z_s	14.54	-10.79 ± 0.12
LCO/r'	14.68	-10.42 ± 0.21
LCO/i'	14.60	-10.58 ± 0.16
LCO/g'	14.80	-10.09 ± 0.32
LCO/V	14.74	-10.29 ± 0.26
LCO/R	14.67	-10.41 ± 0.20
LCO/B	14.84	-9.99 ± 0.37
UVIT/Silica	15.24	< -9.26
UVIT/Sapphire	15.27	< -8.46
UVIT/BaF2	15.29	< -8.91
UVIT/CaF2-1	15.31	< -8.76
X-ray/1 keV	17.39	-8.31 ± 0.02
X-ray/10 keV	18.38	-10.05 ± 0.04
X-ray/50 keV	19.10	-10.14 ± 0.05

Extinction curve for GX 339–4

The extinction values adopted along the sight-line to GX 339–4 are listed in Table A1 as a function of wavelength, together with the extinction curve (A_λ/A_V). An A_V value of 3.5 mag is assumed, together with a systematic 1σ uncertainty of 0.5 mag (P. Gandhi et al. 2011b; M. Heida et al. 2017; A. A. Zdziarski et al. 2019). The optical regime utilizes the extinction curve of J. A. Cardelli et al. (1989). This is extended to the infrared beyond 1 μm with the extinction curve of J. E. Chiar & A. G. G. M. Tielens (2006), matched at the K band. Extinction values at specific wavelengths of interest corresponding to some filters utilized herein are also noted for ease of reference.

Tabulated spectral energy distribution

Table A2 lists the intrinsic SED relevant for the core across the electromagnetic spectrum. Flux densities refer to the mean, values during our campaign, corrected for reddening and absorption, and plotted in Figs 7 and A2. For the bands with continuous (spectroscopic) coverage in the MIR and X-rays, a few canonical frequencies are tabulated.

Alternative models for the MIR spectral energy distribution

Fig. A2 illustrates the effect on the broad-band SED of replacing the hot-flow component with either a circumbinary disc (left-hand panel), or with a transient soft-state compact jet power-law (right-hand panel). Despite the fact that these can explain the MIR contribution to the SED equally well, neither of these alternative models is favoured, as explained in the main text. The circumbinary disc cannot reproduce the observed MIRI variability characteristics (Section 4.1), while the compact jet mildly over-

Table A3. Archival MIR and quasi-simultaneous X-ray luminosities of black hole XRBs.

Name	MJD	$\log L_{\rm X-ray}$ log erg s^{-1}	$\log L_{\rm MIR}$ log erg s^{-1}	State	d kpc	References
A 0620–00	53454	30.49	31.31	Q	1.5	E. Gallo et al. (2007)
AT 2019wey	59100	35.18	31.52	H	6.0	H.-M. Cao et al. (2022)
	59257	35.03	31.72	H		
	59466	35.18	32.37	H		
	59830	35.27	32.30	H		
	59988	35.33	32.19	H		
	60197	35.12	32.31	H		
	60353	35.32	32.35	H		
GRO J0422 + 32	48874	37.53	34.02	H	2.5	J. Paradijs et al. (1994); C. Brocksopp, R. M. Bandyopadhyay & R. P. Fender (2004)
GRO J1655–40	53636	35.70	33.04	H	3.2	S. Migliari et al. (2007)
GRS 1716–249	56736	38.01	33.12	H	6.9	C. John et al. (2024); J. Casares et al. (2023)
	57864	38.50	33.70	H		P. Saikia et al. (2022)
GRS 1739–278	56736	38.42	33.77	H	7.2	C. John et al. (2024)
GRS 1915 + 105	53280	38.50	34.19	H	9.4	F. Rahoui et al. (2010)
	57125	38.82	34.31	H		
	57662	38.48	34.49	H		
	57854	38.09	34.08	H		
	58386	37.56	33.97	O		
	58750	36.83	34.94	O		
	58954	36.54	34.79	O		
	59114	37.69	34.53	O		
	59317	36.85	34.26	O		
	59681	36.47	34.06	O		
	60047	36.92	35.75	O		
	60101	38.10	35.50	O		G25
	60412	37.13	34.89	O		
GS 1354–64	57245	38.78	34.59	H	25.0	C. John et al. (2024)
GX 339–4	55266	37.89	35.32	H	8.0	P. Gandhi et al. (2011b)
	56816	33.15	32.70	Q		This paper; E. Tremou et al. (2020)
	59828	37.16	34.71	H		D. M. Russell et al. (2022); Tremou et al. (in preparation)
	60379	37.89	33.05	S		This paper
MAXI J0637–430	58923	37.42	31.75	S	8.7	C. John et al. (2024)
MAXI J1348–630	58527	37.98	32.94	S	2.2	
	58690	36.35	32.73	H		
	58892	35.14	32.22	H		
MAXI J1535–571	58008	38.29	34.24	H	4.1	M. C. Baglio et al. (2018)
	58012	38.32	34.65	H		M. C. Baglio et al. (2018)
MAXI J1820 + 070	58258	37.65	34.22	H	2.9	C. Echiburú-Trujillo et al. (2024); J. S. Bright et al. (2025)
	58204	37.88	35.11	H		
	58367	37.63	32.73	S		
	58404	35.85	33.80	H		C. Echiburú-Trujillo et al. (2024); J. S. Bright et al. (2025)
	58568	36.17	34.17	H		
MAXI J1836–194	55845	36.74	35.07	H	8.0	D. M. Russell et al. (2013b); T. D. Russell et al. (2014)
	55861	36.49	34.87	H		D. M. Russell et al. (2013b)
Swift J1357.2–0933	55581	35.52	31.43	H	6.3	C. John et al. (2024); P. Charles et al. (2019)
	56736/55422‡	31.58	32.50	Q		R. M. Plotkin et al. (2016); P. Charles et al. (2019)
Swift J1753.5–0127	55383	36.80	32.73	H	6.0	
	56736	36.39	32.89	S		
	57101	36.36	32.55	S		
	57278	36.42	32.56	S		
	57287	36.48	32.77	H		
V404 Cyg	60231	32.60	32.32	Q	2.2	E. S. Borowski et al. (2025)
V4641 Sgr	56744	36.53	33.20	S	6.2	
	58366	36.67	33.05	H		
	58566	36.59	32.71	H		
	58933	36.79	33.22	S		
XTE J1118+480	51649	35.69	34.45	H	1.7	D. M. Russell et al. (2013); R. J. H. Dunn et al. (2010)
	53331	30.48	30.88	Q		E. Gallo et al. (2007)

Notes. Accretion states: 'Q': Quiescent, 'S': Soft, 'H': Hard. 'O' refers to the X-ray-obscured state specific to GRS 1915+105.
‡X-ray/MIR mean observation dates – non-simultaneous, as may be appropriate for quiescence, to within quiescence variability scatter (e.g. D. M. Russell et al. 2018).
Distances (d) are from Y. Zhao et al. (2023) and J. M. Corral-Santana et al. (2016) and references therein, unless otherwise cited.

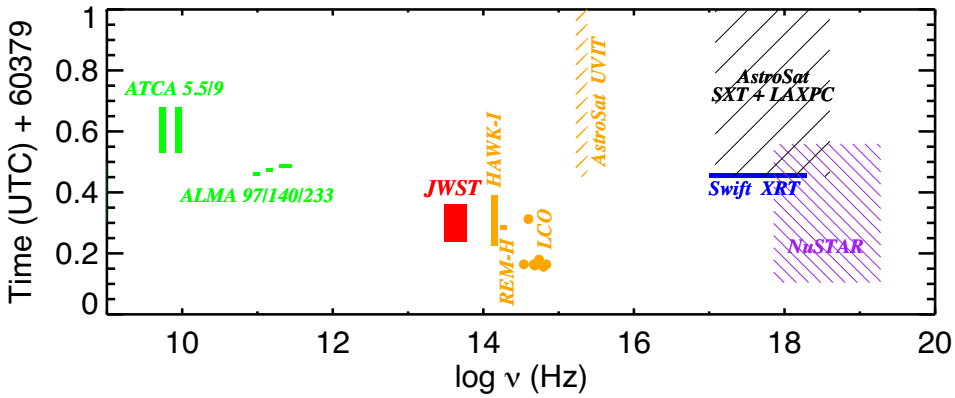

Figure A1. Observation windows across the multiwavelength facilities from our campaign. All observations are continuous within the plotted observing window, except for LCO, which is gappy and the plotted circles denote the mid-observation times; the i' filter was the only LCO filter strictly simultaneous with *JWST*.

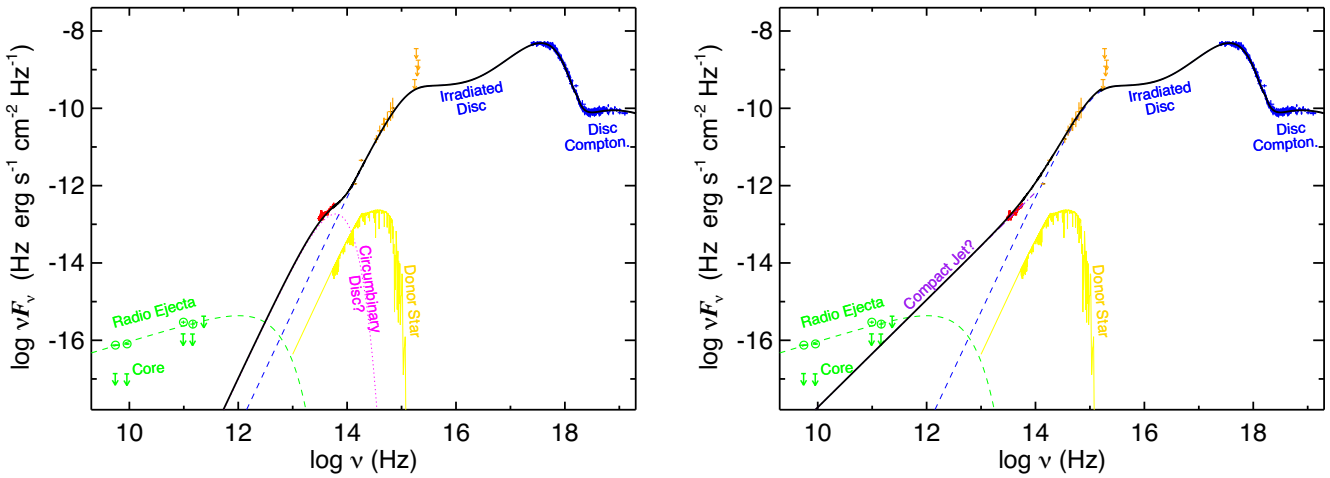

Figure A2. Intrinsic broad-band SED of GX 339–4 in νF_ν units identical in all respects to Fig. 7, except for the physical component dominating the MIR emission: (i) a blackbody simulating a circumbinary disc is shown as the magenta dotted curve on the left; and (ii) a maximal soft-state compact jet fitting the MIRI spectrum is denoted by the purple dot–dashed curve on the right. Either one of these could replace our preferred synchrotron hot flow component based upon the SED alone, but are not preferred for other reasons, as detailed in Section 4.1 and Section 4.4.

produces the observed near-IR emission and also fails to account for the relative X-ray-to-IR variability strengths (Section 4.4).

Archival quasi-simultaneous MIR and X-ray luminosities of black hole XRBs

Table A3 presents the respective MIR and X-ray luminosities of black hole XRBs. This includes all the sources from the extensive compilation of C. John et al. (2024) featuring MAXI and NEOWISE detections (M. Matsuoka et al. 2009; A. Mainzer et al. 2011), supplemented with several other works based on either ground-based MIR detections or detections in the quiescent state, including this paper. Respective references are listed in the table. While this compilation should be fairly comprehensive in terms of MIR-detected sources, we do not claim it to be complete, e.g. there are multiple detections of specific sources such as GRS 1915+105, not all of which are included herein. Multiple detections at very similar joint (overlapping) luminosities are excluded in some cases for plotting purposes. Unless otherwise referenced, the reported luminosities correspond to those from NEOWISE and MAXI from our analysis. Statistical uncertainties are typically $\approx$0.05–0.1 dex, and signal-to-noise values were always better than 3, as also restricted by C. John et al. (2024). Systematic uncertainties (e.g. those on distances discussed below, or on the background and field as discussed for GX 339–4 herein) often dominate for individual objects.

Where energy-band conversions were needed, an X-ray photon-index of $\Gamma = 1.7$ was used to estimate the 0.5–10 keV power. Where NEOWISE data were used, the state assignment follows the band hardness ratios as in C. John et al. (2024); in some cases, there remains ambiguity in hard versus soft states (e.g. for Swift J1753.5–0.127, which plateaued in a hard state for a very extended period), so state definitions should probably be taken with a grain of salt. For the MIR, we chose to report the 8 μm monochromatic luminosity as this should sample the source spectra deep in the thermal infrared within the MIRI band, while still allowing constraints from missions such as *Spitzer* and the tail-end of ground-based observatories sensitive to the so-called '*N*-band' atmospheric window. Any conversions from nearby wavelengths were carried out by using MIR spectral information, where available (e.g. extrapolating the spectral slope between *WISEW*1 and *W*2, or by assuming a flat flux density

$F_\nu \propto \nu^0$ where not). Such band conversions are not perfect, e.g. they do not account properly for obscuration, nor for new spectral components dominating in different MIR bands. On the scale of plot, however, such differences will be minor in most cases. In selected sources such as GRS 1915+105, we cannot rule out systematic differences related to its recent deep X-ray-obscured state, which could introduce scatter of 1–2 dex in its inferred X-ray powers.

We used the custom *WISE* processing results from C. John et al. (2024) where available, except in a few instances where we downloaded and analysed reported catalogue values from the NEOWISE survey (A. Mainzer et al. 2011) for cross-checking or supplementing with newer data that have become available after publication of the results reported by C. John et al. Our results were broadly consistent with published values, with one caveat regarding the distances.

Distances are mostly taken from the recent compilation of XRBs from Y. Zhao et al. (2023), or from J. M. Corral-Santana et al. (2016) and references therein. In three cases, a new and significantly distance measurement results in qualitatively different inferences. These are GRS 1716–249 for which J. Casares et al. (2023) report a best-estimate distance of 6.9 kpc. Swift J1357.2–0933 with a distance of 6.3 kpc (P. Charles et al. 2019) and 6.0 kpc for AT 2019wey (H.-M. Cao et al. 2022). These are all significantly larger than the values assumed in C. John et al. (2024), and move their location to the upper right in the the MIR/X-ray luminosity plane, as discussed in the main text. Other relatively minor changes (including the distance of 8.0 kpc for GX 339–4 used herein, as compared to 5.0 kpc in C. John et al.) have a much smaller impact on the overall distribution. Furthermore, we stress that some of our assumed distances are likely still lower limits (e.g. Swift J1357.2–0933 and AT 2019wey), which may change their location further with updated studies.

Only observations that are simultaneous in X-rays and MIR to within 1 d are retained for the hard as well as soft states. For the quiescent state, flux variations by orders of magnitude are unlikely, and we include non-simultaneous data in one instance for source Swift J1357.2–0933. Excluding this data point does not change any of our inferences qualitatively.

[1]*School of Physics and Astronomy, University of Southampton, Southampton SO17 1BJ, UK*
[2]*Center for Astrophysics and Space Science, New York University, Abu Dhabi, PO Box 129188, Abu Dhabi, UAE*
[3]*INAF – Osservatorio Astronomico di Brera, Via Bianchi 46, I-23807 Merate (LC), Italy*
[4]*Department of Astronomy and Astrophysics, Tata Institute of Fundamental Research, 1 Homi Bhabha Road, Colaba, Mumbai 400005, India*
[5]*INAF – Osservatorio Astronomico di Cagliari, Via della Scienza 5, I-09047 Selargius (CA), Italy*
[6]*Anton Pannekoek Institute for Astronomy and Gravitation Astroparticle Physics Amsterdam (GRAPPA) Institute*
[7]*University of Amsterdam, Science Park 904, NL-1098XH Amsterdam, the Netherlands*
[8]*Department of Physics, University of Alberta, CCIS 4-181, Edmonton, AB T6G 2E1, Canada*
[9]*Space Telescope Science Institute, 3700 San Martin Drive, Baltmore, MD 21218, USA*
[10]*Eureka Scientific Inc., 2542 Delmar Avenue, Suite 100, Oakland, CA 94602-30414, USA*
[11]*Department of Physics & Astronomy, Texas Tech University, Box 41051, Lubbock, TX 79409-1051, USA*
[12]*Dipartimento di Fisica, Università degli Studi di Milano, Via Celoria 16, I-20133 Milano, Italy*
[13]*INAF – IASF Palermo, via Ugo La Malfa, 153, I-90146 Palermo, Italy*
[14]*Department of Physics & Astronomy, Butler University, 4600 Sunset Avenue, Indianapolis, IN 46208*
[15]*Department of Physics and Astronomy, University of Lethbridge, Lethbridge, AB T1K 3M4, Canada*
[16]*INAF Istituto di Astrofisica e Planetologia Spaziali, Via del Fosso del Cavaliere 100, I-00133 Roma, Italy*
[17]*Department of Physics & Astronomy, Louisiana State University, 202 Nicholoson Hall, Tower Drive, Baton Rouge, LA 70803, USA*
[18]*South African Astronomical Observatory, P.O.Box 9, Observatory 7935, South Africa*
[19]*INAF – Osservatorio Astronomico di Roma, via Frascati 33, I-00078 Monteporzio Catone (RM), Italy*
[20]*Inter-University Centre for Astronomy and Astrophysics, Post Bag 4, Ganeshkhind, Pune 411007, India*
[21]*Space Sciences Laboratory, University of California, 7 Gauss Way, Berkeley, CA 94720-7450, USA*
[22]*Faulkes Telescope Project, Cardiff, UK*
[23]*The Schools' Observatory, Liverpool John Moores University, IC2, 146 Brownlow Hill, Liverpool L3 5RF, UK*
[24]*Department of Physics, Centre for Extragalactic Astronomy, Durham University, South Road, Durham DH1 3LE, UK*
[25]*Department of Physics, R. J. College, Mumbai 400086, India*
[26]*Jet Propulsion Laboratory, California Institute of Technology, 4800 Oak Grove Drive, Pasadena, CA 91109, USA*
[27]*Instituto de Astrofisica de Canarias (IAC), E-38200 La Laguna, Tenerife, Spain*
[28]*Departamento de Astrofisica, Universidad de La Laguna (ULL), E-38206 La Laguna, Tenerife, Spain*

This paper has been typeset from a TEX/LATEX file prepared by the author.